



ARTICLE

Persistent DNA damage signaling and DNA polymerase theta promote broken chromosome segregation

Delisa E. Clay¹, Heidi S. Bretscher², Erin A. Jezuit², Korie B. Bush³, and Donald T. Fox^{1,2,3}

Cycling cells must respond to DNA double-strand breaks (DSBs) to avoid genome instability. Missegregation of chromosomes with DSBs during mitosis results in micronuclei, aberrant structures linked to disease. How cells respond to DSBs during mitosis is incompletely understood. We previously showed that *Drosophila melanogaster* papillar cells lack DSB checkpoints (as observed in many cancer cells). Here, we show that papillar cells still recruit early acting repair machinery (Mre11 and RPA3) and the Fanconi anemia (FA) protein Fancd2 to DSBs. These proteins persist as foci on DSBs as cells enter mitosis. Repair foci are resolved in a stepwise manner during mitosis. DSB repair kinetics depends on both monoubiquitination of Fancd2 and the alternative end-joining protein DNA polymerase θ . Disruption of either or both of these factors causes micronuclei after DNA damage, which disrupts intestinal organogenesis. This study reveals a mechanism for how cells with inactive DSB checkpoints can respond to DNA damage that persists into mitosis.

Introduction

Cells are constantly at risk for DNA damage from internal and external factors (Cannan and Pederson, 2016) and respond to such damage to maintain genome stability (Ciccio and Elledge, 2010; Harper and Elledge, 2007). DNA lesions trigger DNA damage response (DDR) checkpoints that result in cell-cycle arrest, DNA repair, or apoptosis (Jackson and Bartek, 2009; Petsalaki and Zachos, 2020). DDR checkpoints primarily act in interphase but allow for faithful chromosome segregation when damaged cells enter mitosis (Finn et al., 2012; Sekelsky, 2017). If cell cycle checkpoints are inactivated or dysregulated, damaged DNA can persist into mitosis (Hafner et al., 2019; Santivasi and Xia, 2014). One of the more problematic forms of persistent DNA damage for the mitotic cell are double-strand breaks (DSBs), which can lead to missegregation and subsequent loss of portions of the genome (Aleksandrov et al., 2020; Vignard et al., 2013). DSBs generate acentric DNA, a DNA fragment that lacks canonical kinetochore-spindle attachments and is at risk of missegregating in mitosis, which can lead to micronuclei, aberrant nuclear structures with a poorly formed nuclear envelope (Bretscher and Fox, 2016; Crasta et al., 2012; Durante and Formenti, 2018).

However, acentric DNA can segregate properly in several organisms, including yeast, *Drosophila melanogaster*, and human

cells (Warecki and Sullivan, 2020). In *Schizosaccharomyces pombe*, acentric DNA can segregate in mitosis by forming a neocentromere and by noncanonical DNA repair (Ishii et al., 2008; Ohno et al., 2016). In *Caenorhabditis elegans*, acentric meiotic chromosomes are thought to segregate by poleward microtubule-generated forces (Dumont et al., 2010). In *D. melanogaster* brain progenitors, acentric DNA can segregate poleward in mitosis by using various mechanisms involving protein-based tethers, microtubule forces, nuclear envelope reformation and fusion, and recruitment of early acting repair proteins (Derive et al., 2015; Karg et al., 2015, 2017; Landmann et al., 2020; Royou et al., 2010; Warecki et al., 2020). Therefore, several proposed mechanisms exist for how acentric DNA properly segregates in mitosis under distinct conditions.

Despite the multiple mechanisms of acentric DNA segregation, questions still remain surrounding possible physical connections that might link the acentric fragment to segregating, centromeric DNA. More specifically, DNA damage signaling could potentially regulate such a linkage or influence segregation of acentric DNA. We established *D. melanogaster* hindgut rectal papillar cells (hereafter referred to as papillar cells) as an accessible model to understand cellular responses to damaged, acentric DNA that is present in mitosis (Bretscher and Fox,

¹Department of Cell Biology, Duke University School of Medicine, Durham, NC; ²Department of Pharmacology and Cancer Biology, Duke University School of Medicine, Durham, NC; ³University Program in Genetics and Genomics, Duke University School of Medicine, Durham, NC.

Correspondence to Donald T. Fox: don.fox@duke.edu.

© 2021 Clay et al. This article is distributed under the terms of an Attribution-Noncommercial-Share Alike-No Mirror Sites license for the first six months after the publication date (see <http://www.rupress.org/terms/>). After six months it is available under a Creative Commons License (Attribution-Noncommercial-Share Alike 4.0 International license, as described at <https://creativecommons.org/licenses/by-nc-sa/4.0/>).

2016). We previously found that papillar cells inactivate DSB checkpoint responses at a specific developmental time point. At the second larval instar (L2) stage, papillar cells undergo two rounds of endocycling (Fox and Duronio, 2013; Øvrebø and Edgar, 2018) where they replicate genome content without cell division (Fig. 1 A, L2). During this stage, papillar cells do not arrest the cell cycle or undergo apoptosis in response to high levels of DNA damage (20-Gy x-ray irradiation [IR]) as in other endocycling cells (Calvi, 2013; Hassel et al., 2014; Mehrotra et al., 2008). Papillar cells do not respond to changes in p53 expression or depend on the checkpoint kinases Chk1 and Chk2 following DNA damage (Bretscher and Fox, 2016). Despite inactivating canonical DSB responses, several (5–6) days later during the early pupation stage, papillar cells leave a G2-like state and enter a mitotic cell cycle (Fig. 1 A, early pupal; Fox et al., 2010; Stormo and Fox, 2016, 2019). As a consequence, papillar cells frequently enter mitosis with acentric DNA fragments (~12% of divisions; Bretscher and Fox, 2016). Despite papillar cell acentric DNA lacking obvious physical connections, these fragments lag but ultimately segregate into daughter nuclei (Fig. 1 A, mitotic). We identified that papillar cell acentric DNA segregation requires proteins from the Fanconi anemia (FA) pathway, Fancd2 and Fanci (Bretscher and Fox, 2016).

In the current study, we further investigate the mechanism of acentric DNA segregation to better understand the possible linkage of acentric fragments to centromeric DNA during mitosis. We find that despite lacking a canonical DDR, papillar cells recruit early acting repair proteins from the MRN (Mre11) and RPA (RPA3) complexes as well as from Fancd2 to DSBs. These proteins persist on damaged papillar chromosomes for days (5–6 d) following DSBs and remain present as these cells enter mitosis. During mitosis, repair protein kinetics are distinct, with Mre11 and Fancd2 leaving the DNA before RPA3. Furthermore, we find that the alternative end-joining (alt-EJ) repair protein DNA polymerase θ (Pol θ ; encoded by the *polQ* gene), but not homologous recombination (HR) or canonical homologous end-joining (cNHEJ), is required for RPA3 removal during mitosis, for acentric DNA segregation, and for micronuclei prevention. Finally, we show that *polQ* RNAi is epistatic to mutants lacking the conserved monoubiquitination site of Fancd2. The actions of Mre11, Pol θ , and monoubiquitinated Fancd2 are critical for intestinal organogenesis following DSBs. Our findings highlight a role for persistent DNA repair signaling, regulated by a conserved alt-EJ protein and monoubiquitinated Fancd2, on acentric DNA.

Results

Mre11 and RPA3 are recruited to damaged papillar chromosomes but are not resolved before mitosis

Although papillar cells lack apoptotic and cell-cycle arrest responses to DNA damage, it remained possible that these cells activate DNA repair responses to segregate acentric DNA. To visualize DNA repair signaling dynamics, we investigated the temporal recruitment of early acting DNA damage repair proteins following DSBs. The highly conserved MRN (Mre11, Rad50, Nbs) complex is recruited immediately to DSBs and initiates

downstream repair events (Petsalaki and Zachos, 2020; Syed and Tainer, 2018; Tisi et al., 2020). We assayed localization of Mre11 over time using animals expressing *ubi-mre11-GFP* (Landmann et al., 2020). We used an established method to induce DSBs, the endonuclease *hs-I-CreI*, which creates DSBs in the rDNA of the *D. melanogaster* sex chromosomes, to increase the frequency of papillar cells with acentric DNA from 12% up to 90% (Bretscher and Fox, 2016; Rong et al., 2002; Royou et al., 2010).

As a control for mitotic cycling cells with an intact DSB response, we examined L3 stage brain progenitor cells (neuroblast and ganglion mother cells; Fig. 1 A'; Jaklevic et al., 2006; Peterson et al., 2002; Royou et al., 2005). In brain progenitors, Mre11⁺ foci are recruited shortly (<30 min) after *hs-I-CreI* DSB induction (Fig. 1, B and B' vs. Fig. 1, C, C', and L). These foci are mostly resolved 24 h after DNA damage, suggesting that repair is complete within this time frame (Fig. 1, C-F' and L). Consistent with this idea, 24 h after DNA damage, we observe mitotic neural progenitors, suggesting that these cells begin to exit cell-cycle arrest (data not shown). Similar to our findings in brains, checkpoint-inactive papillar cells recruit Mre11⁺ foci <30 min after inducing DSBs (Fig. 1, G and G' vs. Fig. 1, H, H', and M). However, these foci persist for much longer than in larval brain progenitors (Fig. 1, H-K and M). During early pupation, several days after we induce DSBs, Mre11⁺ foci still persist on damaged papillar chromosomes. The long time frame of Mre11 persistence corresponds with the 5–6-d period between papillar cell endocycles and the first mitosis, which occurs 24 h after pupation onset (Fig. 1 A; Bretscher and Fox, 2016). Thus, although an MRN component is promptly recruited to checkpoint-inactive papillar cells shortly after a DSB, this protein persists on broken DNA into mitosis.

We next investigated whether Mre11 recruitment coincides with and recruits other markers of DSB repair. Mre11⁺ foci in both brain and papillar cells colocalize with gH2Av, a hallmark of DSB signaling (Fig. S1, A–B' and D–E'). Mre11 and gH2Av do not always colocalize (Fig. S1 G). Similar Mre11 kinetics have been observed in other studies and likely reflects dynamic repair signaling over time (Furuta et al., 2003; Nakamura et al., 2010). MRN binds to either side of a DSB, then recruits downstream repair factors of different DSB repair pathways. MRN can also initiate DNA resection in which 5' DNA ends are processed, leaving 3' single-strand DNA overhangs. These 3' overhangs are coated by the heterotrimeric complex RPA, which prevents annealing of single-strand DNA (Syed and Tainer, 2018; Tisi et al., 2020).

To determine whether MRN recruits RPA in papillar cells after DNA damage, we used animals expressing *ubi-RPA3-GFP* (Murcia et al., 2019). Similar to Mre11, RPA3⁺ foci are present <30 min after *hs-I-CreI*-induced DSBs in larval brain progenitors (Fig. 2, A and A' vs. Fig. 2, B, B', and D). These foci are resolved 24 h after DNA damage (Fig. 2, C, C', and D). RPA3⁺ foci also appear in papillar cells <30 min after *hs-I-CreI*-induced DSBs (Fig. 2, E and E' vs. Fig. 2, F, F', and J). However, unlike in neural progenitors, RPA3 foci are not resolved by 24 h (Fig. 2, G, G', and J) and persist 4–5 d after DNA damage (Fig. 2, H, H', and J), similarly to Mre11. Persistent RPA3 is not due to GFP tagging

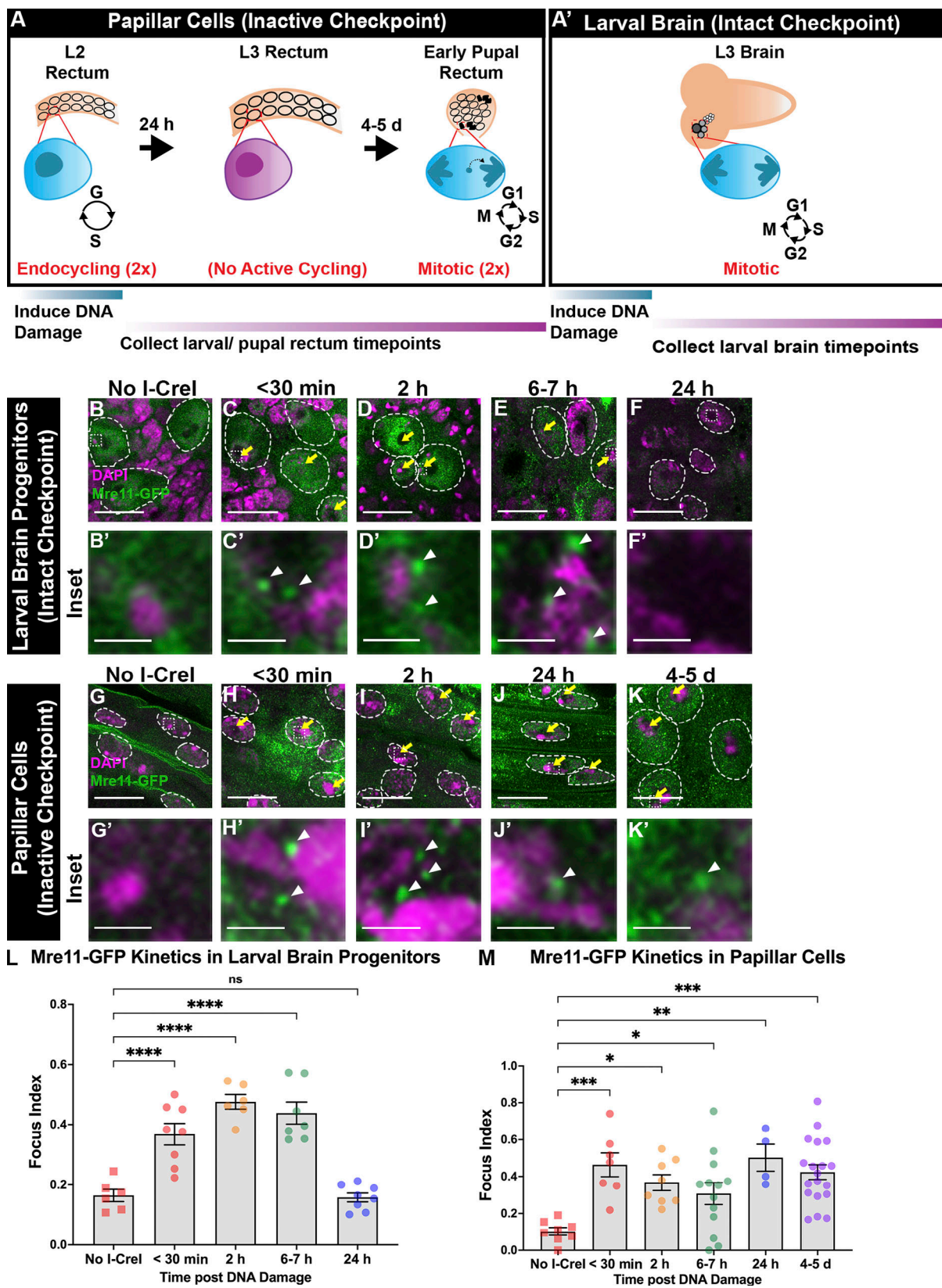


Figure 1. **Mre11 is recruited to checkpoint inactivated papillar cells and persists for days.** (A) Schematic of the developing *D. melanogaster* rectum from the L2 stage to early pupation. (A') Schematic of the feeding L3 brain. Dark gray circles, neuroblasts; gray circles, ganglion mother cells; white circles, neurons (see Results). (B–K') Mre11-GFP localization over time \pm *hs-I-Crel* in larval brain progenitors (B–F') and papillar cells (G–K'). Green, Mre11; magenta, DNA (DAPI); yellow arrows, Mre11⁺ foci; dashed outlines, nuclei; dashed box, area magnified $\times 10$ in the corresponding inset; white arrowheads, enlarged foci. Scale bars = 10 μ m; inset scale bars = 0.5 μ m. (L) Quantification of Mre11⁺ foci kinetics in larval brain progenitors (No *I-Crel*, 334 cells, six animals; <30 min, 770 cells, eight

animals; 2 h, 474 cells, six animals; 6–7 h, 629 cells, seven animals; 24 h, 845 cells, eight animals; $P < 0.0001$). **(M)** Quantification of Mre11⁺ foci kinetics in papillar cells (No *I-CreI*, 1,185 cells, 8 animals; <30 min, 813 cells, 7 animals; 2 h, 857 cells, 8 animals; 6–7 h, 1,264 cells, 13 animals; 24 h, 527 cells, 4 animals; 4–5 d, 1,669 cells, 19 animals; $P = 0.0002$). Focus index was determined as the percentage of cells with at least one DNA repair focus. Individual foci were not counted due to somatic chromosome pairing in which foci in these cells can coalesce into a single focus. Each time point represents two or more biological replicates. Each data point represents a single animal. Error bars indicate SEM. *, $P < 0.05$; **, $P < 0.01$; ***, $P < 0.001$; ****, $P < 0.0001$ by ordinary one-way ANOVA with Dunnett's multiple comparison test.

RPA3 as we observe similar persistent foci with an RPA antibody (Fig. 2 K). Furthermore, persistent RPA foci colocalize with gH2AV, indicating that foci represent sites of DSB signaling (Fig. 2 K). We then determined whether Mre11 recruits RPA3 to papillar DSBs. We examined *ubi-RPA3-GFP* in animals expressing *UAS-mre11* RNAi, which was expressed by the pan-hindgut driver *byn>GAL4* (Iwaki and Lengyel, 2002). RPA3⁺ foci are significantly decreased in *mre11* RNAi papillar cells (Fig. 2 I, I', and J). These data suggest that RPA3 is recruited to papillar chromosomes in an Mre11-dependent manner in response to DSBs.

Using other DSB strategies, we confirmed that RPA3 recruitment and persistence in papillar cells is not specific to *hs-I-CreI*-induced DSBs in rDNA. Using IR (20 Gy) to induce randomly located DSBs, persistent Mre11 and RPA3⁺ foci form on papillar cell DNA compared with quickly resolved foci in larval brain progenitors (Fig. S1, C, F, H, and I). *I-CreI* targets repetitive heterochromatin, and DSB responses can vary based on chromatin state (Chiolo et al., 2011; Dialynas et al., 2019; Rong et al., 2002). We therefore tested whether a single break in a defined euchromatic locus also recruits persistent RPA3 in papillar cells. We used CRISPR-Cas9 to generate DSBs at the *rosy* (*ry*) locus (Carvajal-Garcia et al., 2021). By using this method, we find that RPA3⁺ foci persist in papillar cells (Fig. S1, J and K), similar to our results with *hs-I-CreI*. Foci recruitment occurs both in the DAPI-bright heterochromatin and in other nuclear sites (Fig. S1 L). Overall, our results are consistent with immediate recruitment of Mre11, which recruits RPA3, after DSBs in papillar cells. Unlike checkpoint-intact neural progenitors, these repair markers persist on damaged DNA during a long interphase and continue into mitosis.

Mre11 is required for acentric DNA segregation and cell survival following DNA damage

To determine the function of persistent Mre11 following DSBs in papillar cells, we induced *hs-I-CreI* during the L2 stage, when papillar cells are endocycling and suppressing canonical DNA damage checkpoints (Fig. 3 A). Then, using *byn>GAL4*, we expressed *UAS-mre11* RNAi in the fly hindgut (Fig. 3 A). Following two rounds of mitoses during pupal development, four papillar structures made up of ~100 cells each are present in the adult animal (Cohen et al., 2020; Fox et al., 2010). We previously found that *fancd2* RNAi decreases adult papillar cell number after DSB induction following failure to segregate acentric DNA. In contrast, no cell number reduction occurs in *p53* null mutants or in *chk1*, *chk2* double mutants (Bretscher and Fox, 2016). Similar to our previous findings with *fancd2* RNAi, *mre11* RNAi adult animals contain a significantly reduced number of adult papillar cells and have aberrantly shaped papillae following *hs-I-CreI* (Fig. 3, B and C).

By using fixed and in vivo live imaging, we followed the fate of acentric DNA in the first mitosis following DSBs (Fig. 3 D), using *H2Av-GFP* to label DNA and *CenpC-Tomato* to mark centromeres/kinetochores. Previously, we found that failed acentric DNA segregation in papillar cells leads to acentric micronuclei, as occurs in *fancd2* RNAi animals (Bretscher and Fox, 2016). Similarly, *mre11* RNAi results in an inability to properly segregate acentric DNA during papillar cell mitosis, leading to an increase in acentric micronuclei (Fig. 3, E and F). We note that in addition to accumulating acentric micronuclei, *mre11* RNAi increases anaphase bridges between centromere-containing chromosomes in both *hs-I-CreI* (Fig. 3 E, arrowheads) and no *hs-I-CreI* animals (data not shown). This is likely due to the Mre11 function in telomere maintenance (Syed and Tainer, 2018). To focus on acentric DNA, we only counted micronuclei that lacked a CenpC signal, as acentric fragments do not express this marker. We conclude that Mre11 is required to properly segregate acentric DNA during mitosis, subsequent cell survival, and normal papillar organogenesis.

Mre11 and RPA3 have distinct localization patterns at DSBs during mitosis

As acentric fragments fail to properly incorporate during mitosis after *mre11* knockdown, we next examined Mre11 dynamics specifically in the first mitosis after DSBs. We live imaged rectums expressing *H2Av-RFP* and *ubi-mre11-GFP* during the early (24-h postpuparium formation) pupal stage. Compared with papillar cells without *hs-I-CreI* DSBs, Mre11⁺ foci persist on papillar chromosomes at a significantly higher frequency during early prophase (Fig. 4 A [-17:00] and Fig. 4 B). After nuclear envelope breakdown (NEBD), Mre11⁺ foci are resolved (Fig. 4 A [00:00] and Fig. 4 B). Therefore, Mre11⁺ foci are apparent at DSBs in <30 min, persist for days on broken papillar chromosomes until early mitosis, and resolved by NEBD.

As RPA3 is recruited downstream of Mre11 (Fig. 2, I and J), we next examined RPA3 localization during the first mitosis after induced DSBs. We live imaged *H2Av-RFP* and *ubi-RPA3-GFP* in mitotic papillar cells. Similar to Mre11, RPA3⁺ foci are found on mitotic papillar chromosomes after *hs-I-CreI* DSBs (Fig. 4 C [-11:00] and Fig. 4 D). However, RPA3 differs from Mre11 in that *hs-I-CreI*-induced RPA3⁺ foci are found at an increased level through prophase (Fig. 4, C and D). Following prophase, the mean RPA3 focus index (the frequency in which a cell contains at least one RPA3 focus) decreases (Fig. 4 D), although a subset of cells contain RPA3⁺ foci on lagging DNA fragments during anaphase (Fig. 4 C [25:00]). RPA3⁺ foci are mostly resolved by the following interphase after mitosis (Fig. 4 C [40:00]). This gradual RPA3 loss beginning at metaphase may reflect the onset

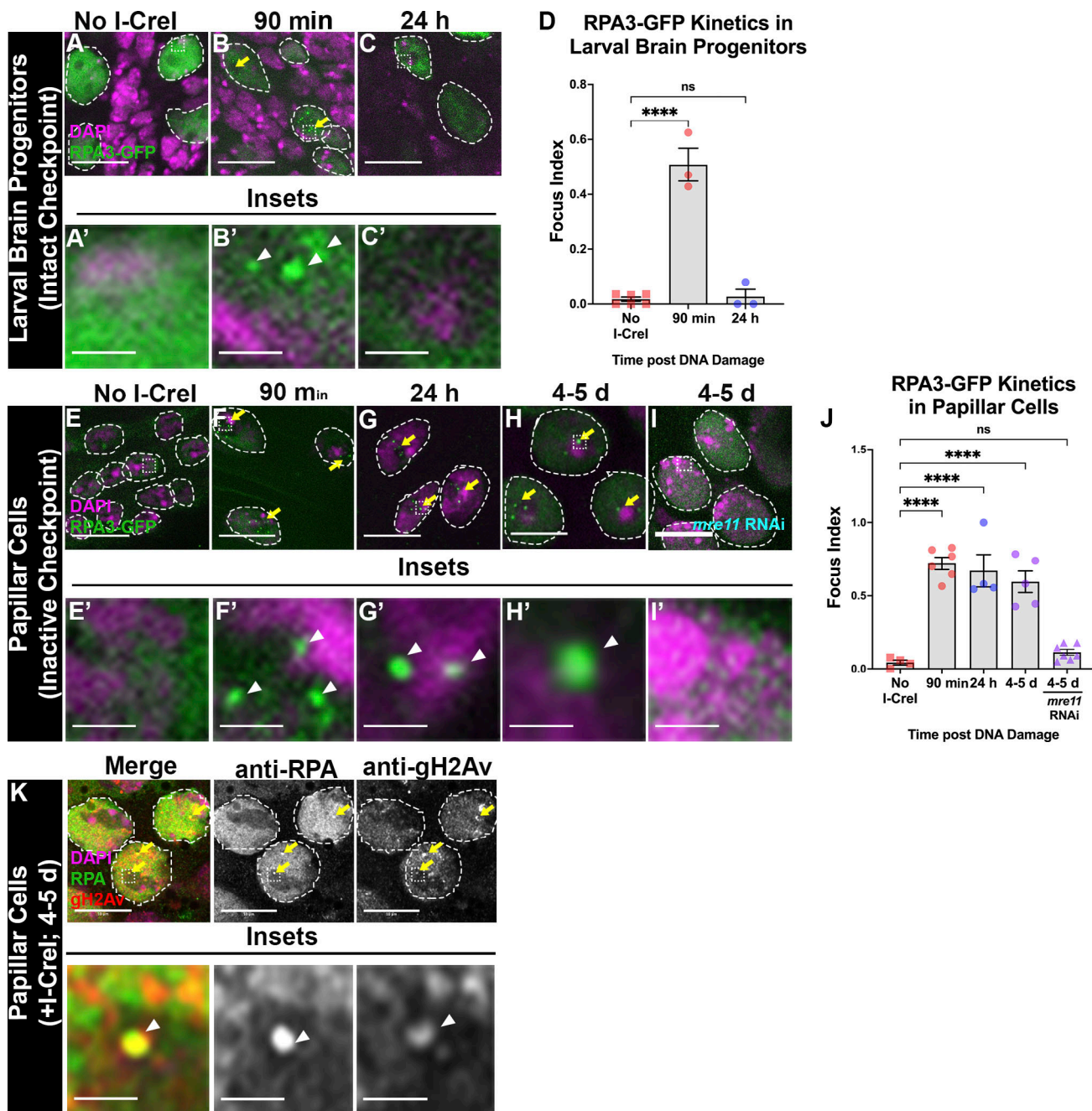


Figure 2. RPA3 is recruited to checkpoint inactive papillar cells and persists for days. (A–C' and E–I') RPA3-GFP localization over time \pm *hs-I-Crel* in larval brain progenitors (A–C'), WT papillar cells (E–H'), and *mre11* RNAi papillar cells (I and I'). Green, RPA3; magenta, DNA (DAPI); yellow arrows, RPA3⁺ foci; dashed outlines, nuclei; dashed box, area magnified $\times 10$ in the corresponding inset; white arrowheads, enlarged foci. Scale bars = 10 μ m; inset scale bars = 0.5 μ m. **(D)** Quantification of RPA3⁺ foci kinetics in larval brain progenitors (No *I-Crel*, 200 cells, six animals; 90 min, 48 cells, three animals; 24 h, 63 cells, three animals; $P < 0.0001$). **(J)** Quantification of RPA3⁺ foci kinetics in papillar cells (No *I-Crel*, 139 cells, four animals; 90 min, 108 cells, six animals; 24 h, 81 cells, four animals; 4–5 d, 658 cells, five animals, 4–5 d *mre11* RNAi, 99 cells, seven animals; $P < 0.0001$). Each time point represents two or more biological replicates. Each data point represents a single animal. Error bars indicate SEM. ****, $P < 0.0001$ by ordinary one-way ANOVA with Dunnett's multiple comparison test. **(K)** RPA⁺ gH2Av⁺ foci recruitment to papillar cells 4–5 d + *hs-I-Crel*. Green, RPA; magenta, DNA (DAPI); red, gH2Av; yellow arrows, RPA⁺ gH2Av⁺ foci. All other labeling as in A–I'.

of repair between metaphase and the next interphase (see Discussion). We also assayed the focus intensity, which steadily decreases as cells progress through mitosis (Fig. 4, C and E). We confirmed that similar kinetics are observed when monitoring localization of endogenous RPA (Fig. S1, M and N). We conclude

that Mre11 and RPA3⁺ foci persist into mitosis after DSBs. While Mre11⁺ foci are resolved before NEBD, RPA3⁺ foci continue to persist at high levels until metaphase, and then gradually decrease on broken papillar DNA, resolving fully by the following interphase.

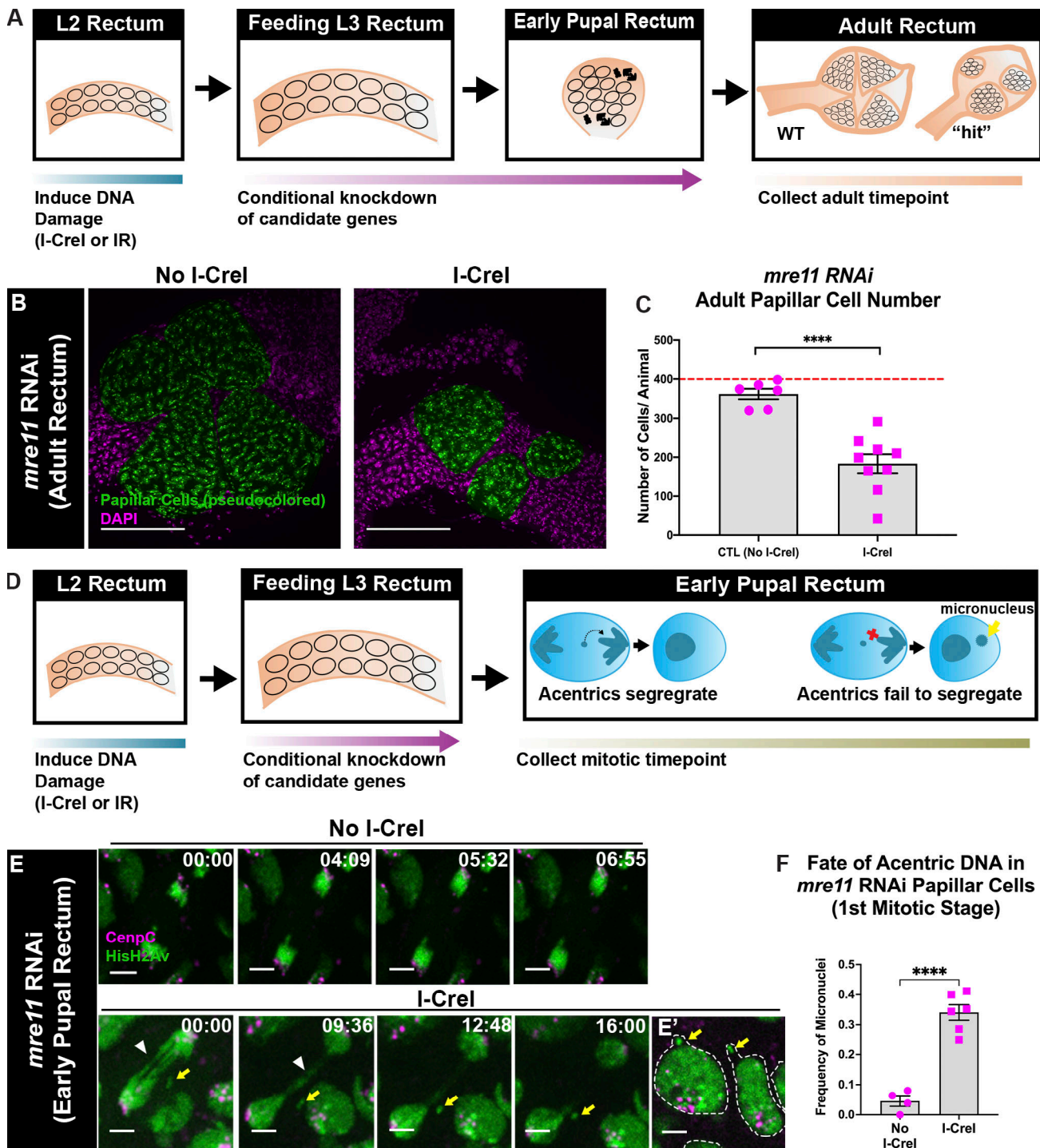


Figure 3. **Mre11 is required for segregation of acentric DNA during mitosis.** (A) Adult candidate screen assay for identifying regulators of acentric DNA segregation based on Bretscher and Fox (2016); see Results. (B) Adult rectums of *mre11* RNAi animals \pm *hs-I-Crel*. Green, papillar cells (pseudocolored); magenta, DNA (DAPI). Scale bars = 50 μ m. (C) Quantification of adult papillar cell number in *mre11* RNAi animals (+ *hs-I-Crel*, 1,652 cells, nine animals; - *hs-I-Crel*, 2,170 cells, six animals; P < 0.0001. Red dashed line indicates the expected number of papillar cells in WT adult. Each condition represents two or more biological replicates. Each data point represents a single animal. Error bars indicate SEM. ****, P < 0.0001 by unpaired two-tailed t test without Welch's correlation. (D) Pupal candidate screen assay for identifying regulators of acentric DNA segregation based on Bretscher and Fox (2016); see Results. (E) Live imaging of papillar cell mitosis in *mre11* RNAi animals \pm *hs-I-Crel*. Green, HisH2Av; magenta, CenpC; yellow arrow, acentric fragment; white arrowheads, chromatin bridge. Scale bars = 5 μ m. (E') Micronuclei-containing papillar cells following mitosis + *hs-I-Crel* in animals expressing *mre11* RNAi. Dashed outline, nuclei. Labeling and scale bars as in E. (F) Quantification of the fate of acentric fragments in *mre11* RNAi papillar cells (+ *hs-I-Crel*, 317 cells, six animals; - *hs-I-Crel*, 390 cells, four animals). Each condition represents two or more biological replicates. Each data point represents a single animal. Error bars indicate SEM. ****, P < 0.0001 by unpaired two-tailed t test without Welch's correlation. CTL, control.

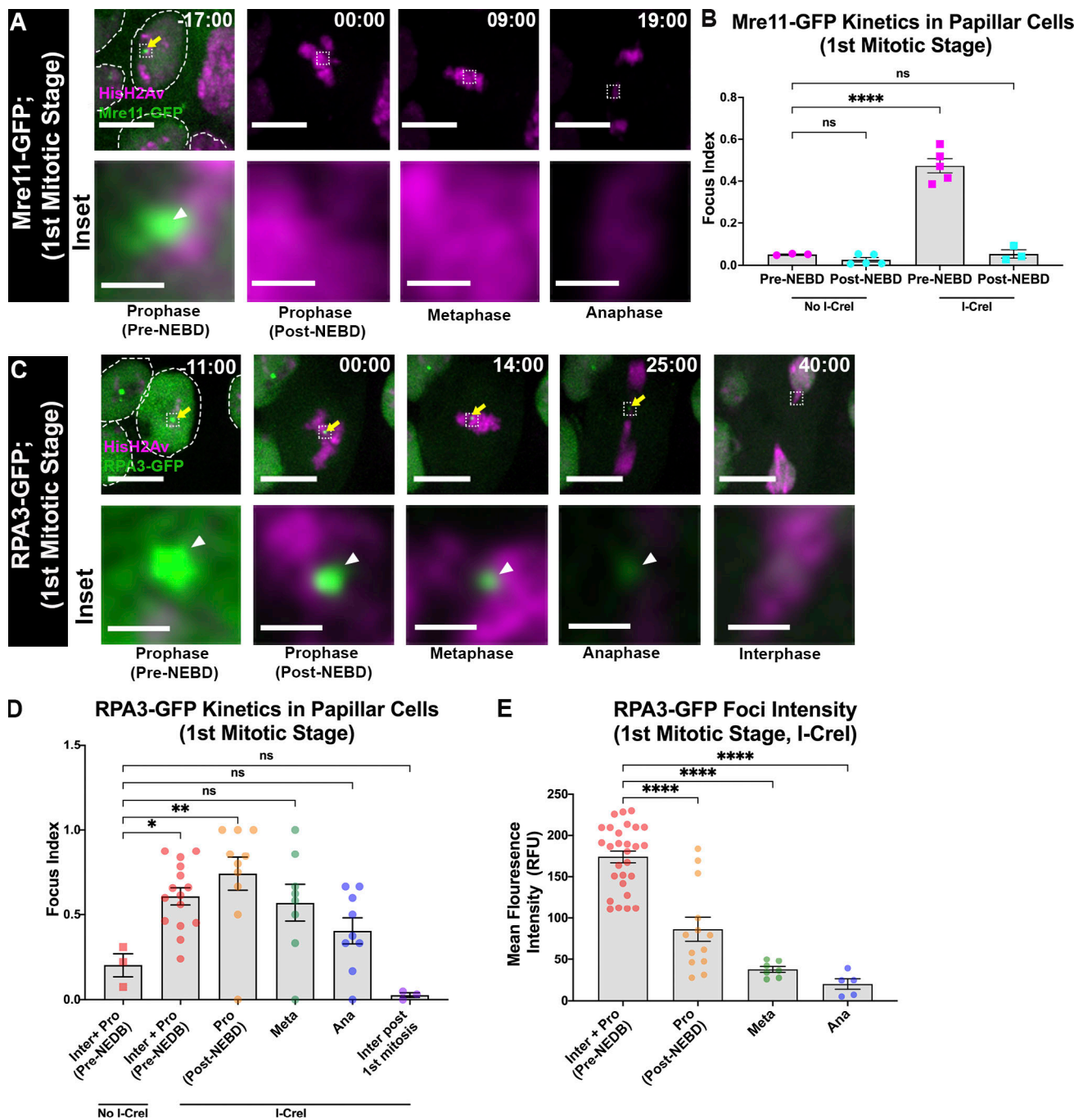


Figure 4. **Mre11 and RPA3 have distinct kinetics during mitosis.** (A and C) Mre11-GFP (A) and RPA3-GFP (C) localization in papillar cells during mitosis \pm *hs-I-Crel*. Green, Mre11/RPA3; magenta, HisH2Av; yellow arrows, Mre11⁺/RPA3⁺ foci; dashed box, area magnified $\times 10$ in the corresponding inset; white arrowheads, enlarged foci. In the $-17:00$ frame, dashed outlines indicate nuclei. Scale bars = 10 μm ; inset scale bar = 0.5 μm . (B) Quantification of the focus index for Mre11⁺ foci kinetics during papillar mitosis (No *I-Crel* pre-NEBD, 410 cells, three animals; No *I-Crel* post-NEBD, 868 cells, five animals; pre-NEBD, 157 cells, five animals; post-NEBD, 235 cells, three animals; $P < 0.0001$). (D) Quantification of the focus index for RPA3⁺ foci kinetics during papillar mitosis (No *I-Crel* interphase [Inter] + prophase [Pro] (pre-NEBD), 146 cells, 3 animals; Inter + Pro (pre-NEBD), 722 cells, 15 animals; Pro (post-NEBD), 51 cells, 10 animals; metaphase [Meta], 50 cells, 8 animals; anaphase [Ana], 49 cells, 9 animals; Inter post first mitosis, 80 cells, 3 animals; $P = 0.0003$). (E) Quantification of RPA3⁺ foci intensity in papillar cells during mitosis \pm *hs-I-Crel* (Inter + Pro (pre-NEBD), 28 cells; Pro (post-NEBD), 13 cells; Meta, 7 cells; Ana, 5 cells; $P < 0.0001$). Each time point represents two or more biological replicates. Each data point represents a single animal except in E, where each data point represents a single cell. Error bars indicate SEM. *, $P < 0.05$; **, $P < 0.01$; ****, $P < 0.0001$ by ordinary one-way ANOVA with Dunnett's multiple comparison test. RFU, relative fluorescence unit.

A candidate genetic screen identifies *polQ* as being required for acentric DNA segregation

The requirement for Mre11 and the dynamic mitotic localization of Mre11 and RPA3 suggested that these proteins might actively signal repair events to segregate acentric DNA. Based on our observations that Mre11 is required for RPA3 recruitment—likely due to DNA resection—we undertook a candidate genetic screen, with the hypothesis that other repair events occur downstream of RPA3 recruitment. Using adult papillar cell number after *hs-I-CreI* DSBs as a readout to identify regulators of acentric DNA segregation during mitosis (Fig. 3 A; Bretscher and Fox, 2016), we screened 80 candidate genes that we hypothesized to be possibly important for acentric DNA segregation (Table S1). We chose candidate genes based either on their known function in DNA repair or on their identification in a previous cell culture-based *D. melanogaster* screen for DSB-responsive genes (Table S1; Kondo and Perrimon, 2011).

Most genes that we interrogated did not disrupt papillar organogenesis following DSBs. Interestingly, we did not identify a requirement for cNHEJ or HR (Ceccaldi et al., 2016; Sekelsky, 2017; Wright et al., 2018). Specifically, knockdown of regulators of cNHEJ *ku70*, *ku80*, and *lig4* (Ceccaldi et al., 2015; Sekelsky, 2017) did not consistently result in a DSB-specific decrease in papillar cell number (Table S1; 5/6 lines tested were not a hit). Furthermore, the requirement and recruitment of resection factors is inconsistent with cNHEJ as this pathway does not require end resection (Chang et al., 2017). Similarly, Rad51, which is required for HR (Ceccaldi et al., 2015; Sekelsky, 2017; Wright et al., 2018), is not required for papillar cell survival after DSBs (Table S1; and Fig. S2, A and B). We do note that there is a significant decrease in *rad51* RNAi papillar cell number without *hs-I-CreI*, suggesting that Rad51 plays a role in papillar organogenesis (Fig. S2, A and B). Additionally, using an antibody for *D. melanogaster*, Rad51, we find that Rad51 is not recruited until the interphase following the first mitosis, is independent of exogenous DNA damage, and depends on Rad51 function (Fig. S2, C and D), validating that we efficiently knocked down Rad51.

Our screen also included regulators of other DSB repair pathways. In contrast to the lack of requirement for cNHEJ and HR, we identified the gene DNA polymerase Q (*polQ*) as a potential candidate for acentric DNA segregation in papillar cells. *polQ* encodes the Pol θ protein, which is critical in alt-EJ, also described as microhomology-mediated end-joining or θ -mediated end-joining (Beagan et al., 2017; Beagan and McVey, 2016; Chan et al., 2010; Hanscom and McVey, 2020; Kent et al., 2015; McVey and Lee, 2008). Pol θ recognizes microhomologies around a DSB and anneals homologous sequences together (Beagan et al., 2017; Beagan and McVey, 2016; Chan et al., 2010; Hanscom and McVey, 2020; McVey and Lee, 2008; Sharma et al., 2015). We identified several other genes implicated in alt-EJ (Table S1, *erc1*, *fen1*, *xpf*) as required for papillar cell survival following DSBs (Ahmad et al., 2008; Liang et al., 2005; Ma et al., 2003; Sharma et al., 2015). As Pol θ is critical in several steps of alt-EJ (Beagan et al., 2017; Beagan and McVey, 2016; Carvajal-Garcia et al., 2021; Chan et al., 2010; Liang et al., 2005; McVey and Lee, 2008; Sekelsky, 2017; Wood and Doublie, 2016), our further analysis focused on *polQ*.

Knockdown of *polQ* using two independent RNAi lines results in both an *hs-I-CreI* and an IR-induced DSB-specific decrease in adult papillar cell number (Fig. 5, A and B; and Fig. S2, E–H). To determine whether the decrease in cell number coincides with an increase in acentric micronuclei, we observed mitotic stage papillar cells in pupae expressing UAS-*polQ* RNAi. Acentric (CenpC-negative) micronuclei increase after *hs-I-CreI* DSBs in animals expressing UAS-*polQ* RNAi (Fig. 5, C and D). To determine the extent to which *polQ* knockdown affects RPA3⁺ foci, we visualized *ubi-RPA3-GFP* in the presence of *polQ* RNAi. RPA3⁺ foci are present both during and before mitosis on broken papillar chromosomes in animals with *polQ* RNAi. However, whereas RPA3⁺ foci are resolved by the following interphase after mitosis in WT animals (Fig. 4 C [40:00] and Fig. 4 D), RPA3⁺ foci persist into the following interphase in animals expressing *polQ* RNAi (Fig. 5, E and F). These data suggest that our candidate screen successfully identified the alt-EJ regulator *polQ* as required for DSB-dependent cell survival in papillar cells. *polQ* is responsible for proper acentric DNA segregation and micronuclei prevention during papillar mitosis and for the removal of RPA3 by the following interphase.

Monoubiquitinated Fancd2 is required for micronuclei prevention and RPA3 removal

Our analysis of *polQ* RNAi papillar cells resembled our previous study of the FA pathway protein Fancd2. In animals expressing UAS-*fancd2* RNAi under the control of *byn*-Gal4, acentric fragments fail to properly incorporate into daughter papillar cell nuclei and instead form micronuclei (Bretscher and Fox, 2016). This increase in micronuclei correlates with decreased papillar cell number and papillar organogenesis defects, the latter seen also in the Fancd2 binding partner FancI.

Fancd2 forms a heterodimer with FancI, and the recruitment and activation of these proteins frequently depend on monoubiquitination on conserved lysine residues by the FA core complex (FancM and FancL in *D. melanogaster*; Marek and Bale, 2006; Rodríguez and D'Andrea, 2017). To determine to what extent Fancd2 depends on its conserved monoubiquitination, we examined adult papillar cell number in FA core complex RNAi animals (Fig. S3, A–D). Knockdown of both FA core complex members *fancm* and *fancI* in the hindgut using multiple independent RNAi lines results in an *hs-I-CreI*-specific decrease in papillar cell number and associated defects in papillar organogenesis (Fig. S3, A–D). In our previous study (Bretscher and Fox, 2016), we used a *fancm* partial deletion allele (*fancm^{del}*) in combination with a deficiency in the *fancm* region and observed an IR-dependent adult papillar cell phenotype but not a significant *hs-I-CreI*-dependent phenotype. Here, we instead find significant *hs-I-CreI*-dependent papillar cell phenotypes for *fancm* with two separate RNAi lines. Taken together with our previous findings for FancI and Fancd2 (Bretscher and Fox, 2016), we conclude that the entire FA pathway is required in *D. melanogaster* papillar cells with DSBs.

To further test whether Fancd2 monoubiquitination is required for papillar cell survival after DSBs, we used two-step CRISPR-mediated homology-directed repair (Yang et al., 2020) to generate a fly where the conserved, endogenous monoubiquitination

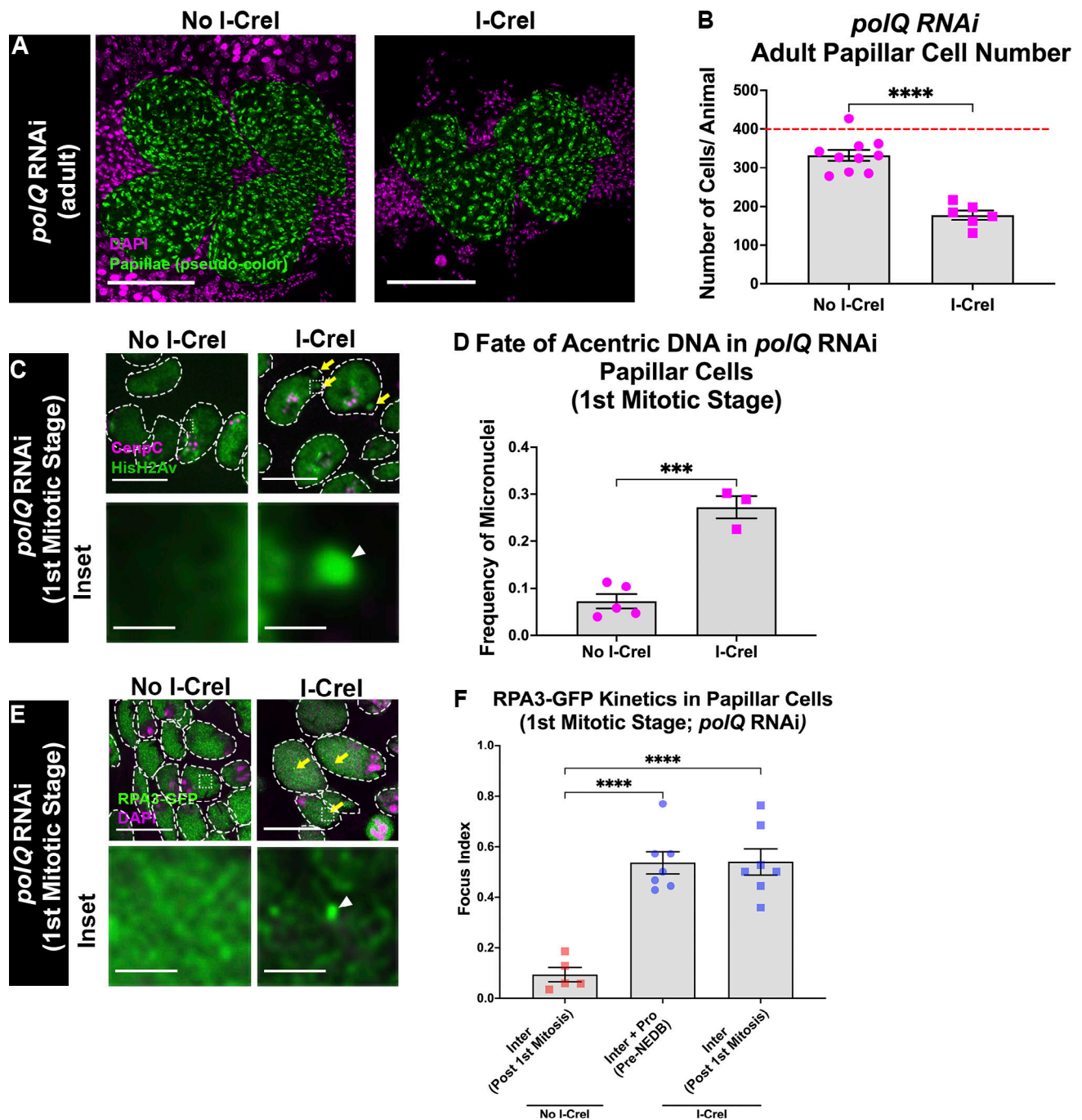


Figure 5. **polQ** is required for proper RPA3⁺ foci dynamics, acentric DNA segregation, and cell survival. **(A)** Adult rectums of *polQ* RNAi animals \pm *hs-I-Crel*. Green, papillar cells (pseudocolored); magenta, DNA (DAPI). Scale bars = 50 μ m. **(B)** Quantification of adult papillar cell number in *polQ* RNAi animals ($+$ *hs-I-Crel*, 1,067 cells, 6 animals; $-$ *hs-I-Crel*, 3,323 cells, 10 animals; $P < 0.0001$). Red dashed line indicates the expected number of papillar cells in WT adult. Each condition represents two or more biological replicates. Each data point represents a single animal. Error bars indicate SEM. ****, $P < 0.0001$ by unpaired two-tailed *t* test without Welch's correlation. **(C)** Still images of live-imaged rectums expressing *polQ* RNAi \pm *hs-I-Crel*. Green, HisH2Av; magenta, CenpC; yellow arrows, micronuclei; dashed outline, nuclei; dashed box, area magnified $\times 10$ in the corresponding inset; white arrowhead, enlarged micronucleus. Scale bars = 10 μ m; inset scale bar = 0.5 μ m. **(D)** Quantification of the fate of acentric fragments in *polQ* RNAi papillar cells ($+$ *hs-I-Crel*, 287 cells, three animals; $-$ *hs-I-Crel*, 175 cells, five animals; $P = 0.0003$). Each condition represents two or more biological replicates. Each data point represents a single animal. Error bars indicate SEM. ***, $P < 0.001$ by unpaired two-tailed *t* test without Welch's correlation. **(E)** RPA3-GFP localization in *polQ* RNAi papillar cells during mitosis \pm *hs-I-Crel*. Green, RPA3; magenta, DAPI; yellow arrows, RPA3⁺ foci. All other labeling as in C. **(F)** Quantification of RPA3⁺ foci kinetics in *polQ* RNAi papillar cells during mitosis \pm *hs-I-Crel* (No *I-Crel* interphase [Inter] + prophase [Pro] (post-NEBD), 175 cells, five animals; Inter + Pro (pre-NEBD), 155 cells, seven animals; Inter post first mitosis, 287 cells, seven animals; $P < 0.0001$). Each time point represents two or more biological replicates. Each data point represents a single animal. Error bars indicate SEM. ****, $P < 0.0001$ by ordinary one-way ANOVA with Dunnett's multiple comparison test.

site for Fancd2, K595, is mutated to an arginine (*fancd2^{K595R}*; Fig. 6 A). This mutation has been previously observed to disrupt monoubiquitination of *D. melanogaster* Fancd2 in vitro (Marek and Bale, 2006). *fancd2^{K595R}* is the first animal model of a mutation in the endogenous conserved monoubiquitination site and the first endogenous *fancd2* mutation of any kind in flies. *fancd2^{K595R}* homozygous animals are viable and fertile, enabling us to test a role for Fancd2 monoubiquitination in acentric DNA responses. *fancd2^{K595R}* animals have decreased adult papillar cell number after both *hs-I-CreI* (Fig. 6, B and C) and IR (Fig. S3, G and H).

We then determined whether Fancd2 monoubiquitination prevents micronuclei. To test this, we measured micronucleus frequency in response *hs-I-CreI* DSBs. In *fancd2^{K595R}* animals, micronucleus frequency is significantly higher in cells with *hs-I-CreI* DSBs compared with *fancd2^{K595R/+}* animals (Fig. 6, D and E). Our findings in previous studies and in the current study support a model where the FA core complex and monoubiquitination of the Fancd2–FancI heterodimer prevent micronuclei during mitosis with DSBs to promote cell survival.

We next examined whether Fancd2 monoubiquitination impacts the dynamic localization of RPA3 after DSBs. To test this, we first visualized *ubi-RPA3-GFP* in animals expressing *fancd2* RNAi. *fancd2* RNAi papillar cells fail to remove RPA3 foci after mitosis following DSBs (Fig. S3, E and F). We then visualized RPA3-GFP in *fancd2^{K595R}* animals. RPA3⁺ foci are recruited to papillar cells before mitosis in response to *hs-I-CreI* DSBs in *fancd2^{K595R}* animals (Fig. 6 G) and animals heterozygous for the K595R mutation (*fancd2^{K595R/+}*; Fig. S3 I). However, DSBs increase the frequency of RPA3⁺ foci in *fancd2^{K595R}* animals following the first mitosis (Fig. 6, F and G). This increased frequency following mitosis is not observed in either WT (Fig. 4, C and D) or *fancd2^{K595R/+}* animals (Fig. S3 I). These findings suggest that similar to Pol θ, conserved Fancd2 monoubiquitination is required to displace RPA3⁺ foci during mitosis.

As monoubiquitinated Fancd2 is not required to recruit RPA3 immediately following DNA damage but is required for RPA3 foci resolution during mitosis, we next investigated the timing of Fancd2 arrival to papillar cells after DSBs. We examined animals expressing *D. melanogaster* Fancd2 tagged with GFP (Fancd2-GFP). Similar to RPA3 and Mre11, papillar cells recruit Fancd2⁺ foci <30 min after *hs-I-CreI* DSBs (Fig. 6 I). Fancd2⁺ foci persist into mitosis but are resolved before NEBD, mirroring Mre11⁺ foci kinetics (Fig. 6, H and I). Taken together, these data suggest that Fancd2 is recruited to RPA3-coated resected DNA shortly after a DSB and recruits downstream repair factors to promote the resolution of RPA3⁺ foci during mitosis.

***polQ* and *fancd2* mutants are epistatic during papillar cell mitosis with DSBs**

Based on the observation that *polQ* and monoubiquitinated Fancd2 are both required for acentric DNA to be incorporated into daughter nuclei during mitosis, we next examined the genetic interaction between these two genes. To test at a genetic level whether *polQ* and monoubiquitinated Fancd2 work in concert to promote papillar cell survival following DNA damage, we knocked down *polQ* using UAS-*polQ* RNAi in *fancd2^{K595R}* animals. After inducing *hs-I-CreI* DSBs during the endocycle, a

significant decrease in adult papillar cell number occurs in *fancd2^{K595R}; polQ* RNAi animals (Fig. 7, A and B). However, we do not observe a significant difference in adult papillar cell number after DSBs in the double-mutant animals compared with either single mutant.

We then determined the effect of *fancd2^{K595R}; polQ* RNAi animals on micronuclei formation during mitosis in papillar cells with *hs-I-CreI* DSBs. The frequency of micronuclei in *fancd2^{K595R}; polQ* RNAi animals increases after DSBs (Fig. 7, C and D). Similar to our findings for adult papillar cell number, we do not observe a significant increase in micronuclei in *fancd2^{K595R}; polQ* RNAi animals relative to either single gene disruption alone (*fancd2^{K595R}* and *polQ* RNAi; Fig. 7 D).

Finally, we examined the ability of *fancd2^{K595R}; polQ* RNAi animals to resolve RPA foci in mitosis. RPA⁺ gH2Av⁺ foci persist following mitosis in papillar cells specifically in response to *hs-I-CreI* DSBs (Fig. 7, E and F). These findings are similar to what we observe in either single mutant. These data suggest that during mitosis with DSBs, *polQ* and monoubiquitinated Fancd2 work in concert to resolve RPA3, prevent micronuclei, and promote papillar cell survival.

Discussion

How DNA repair is regulated in the absence of a *chk1/chk2/p53* checkpoint is incompletely understood. In this study, we find that checkpoint-inactive papillar cells still recruit early acting repair proteins to DSBs (Fig. 7 G). RPA3⁺ repair foci persist into mitosis (Fig. 7 G) but are resolved by the following interphase (Fig. 7 G). RPA3 removal is controlled by Fancd2 and Pol θ (Fig. 7 H). Failure to remove RPA3 correlates with acentric DNA failing to segregate into daughter nuclei, micronuclei, and intestinal organogenesis defects (Fig. 7 H). Based on these findings, we propose that an alt-EJ repair intermediate links the acentric fragment to a broken, centromere-containing chromosome during anaphase, preventing micronuclei and ensuring proper development (Fig. 7, G and G').

A DNA repair intermediate promotes acentric DNA segregation

The recruitment of Mre11, RPA3, and Fancd2 to damaged papillar chromosomes mirrors previous findings, but there are also some distinctions. Following DSBs in checkpoint-inactive papillar cells (this study) and in damaged neuroblasts (Landmann et al., 2020), Mre11 is recruited to DSBs, is dynamic during mitosis, and is required to recruit downstream proteins. While Landmann et al. observed Mre11 recruitment during later mitotic stages than we observe, we note that they induced DSBs in prometaphase instead of before mitosis as performed here. Indeed, timing of DSB induction influences DNA repair (Ceccaldi et al., 2016). Also in the Landmann et al. study, the protein BubR1 is recruited to DSBs. In contrast, our prior study (Bretscher and Fox, 2016) found that papillar cells do not recruit or require BubR1 for acentric DNA segregation. Taken together, our work and findings in *D. melanogaster* neuroblasts highlight the importance of understanding the cellular context in which DSBs arise and how this influences DSB repair.

76 cells, seven animals; Inter post first mitosis, 261 cells, six animals; $P < 0.0001$). Each time point represents two or more biological replicates. Each data point represents a single animal. Error bars indicate SEM. **, $P < 0.01$; ****, $P < 0.0001$ by ordinary one-way ANOVA with Dunnett's multiple comparison test. **(H)** Fancd2-GFP localization to papillar cells during mitosis \pm *hs-I-Crel*. Green, Fancd2; yellow arrows, Fancd2⁺ foci. All other labeling as in D. **(I)** Quantification of Fancd2⁺ foci recruitment in papillar cells \pm *hs-I-Crel* from <30 min to Inter following the first mitotic stage (No *I-Crel* <30 min, 291 cells, five animals; <30 min, 147 cells, four animals; 2 h, 347 cells, four animals; 6 h, 238 cells, six animals; pre-NEBD, 62 cells, four animals; No *I-Crel* pre-NEBD, 55 cells, five animals; post-NEBD, 78 cells, three animals; $P < 0.0001$). Each time point represents two or more biological replicates. Each data point represents a single animal. Error bars indicate SEM. *, $P < 0.05$; **, $P < 0.01$; ***, $P < 0.001$ by ordinary one-way ANOVA with Dunnett's multiple comparison test.

In mammalian cells, micronuclei and chromosomal aberrations are prevented by ultra-fine DNA bridges (UFBs), DNA- and protein-based linkages that need to be resolved during mitosis (Liu et al., 2014). UFBs prevent micronuclei through resolution of replication and repair intermediates by FA proteins, BLM helicase, and RPA2. Similarly, we identified that BLM and Fancd2 are required for acentric DNA segregation in damaged papillar cells, and here, we observe Fancd2 and RPA3 recruitment to damaged papillar chromosomes during mitosis (Fig. 4, C and D; and Fig. 6, H and I; Bretscher and Fox, 2016). We have not observed long RPA3-coated UFBs during mitosis, which we hypothesize to be because papillar cells engage in alt-EJ, which can displace RPA on short microhomology regions around a DSB (Beagan et al., 2017; Beagan and McVey, 2016; Chan et al., 2010; Ciccia and Elledge, 2010; Hanscom and McVey, 2020; Harper and Elledge, 2007; Jackson and Bartek, 2009; Lord and Ashworth, 2012; McVey and Lee, 2008; Sekelsky, 2017). Alt-EJ is a “backup” pathway when major DSB repair pathways are unavailable (Iliakis et al., 2015) in some contexts and is the preferred repair pathway in others (Thyme and Schier, 2016), including during mitosis (Deng et al., 2019; Fernandez-Vidal et al., 2014). We speculate that alt-EJ displaces RPA during mitosis and promotes annealing of broken DNA ends by Pol θ and monoubiquitinated Fancd2 (Fig. 7 G').

Fancd2 monoubiquitination and *polQ* work together to promote acentric DNA segregation

We find that Fancd2 monoubiquitination cooperates with *polQ* to promote acentric DNA segregation. Monoubiquitinated Fancd2 and Pol θ cooperate in other contexts (Kais et al., 2016; Muzzini et al., 2008). Additionally, mutants in Fancd2 and FEN1 (an implicated alt-EJ endonuclease and hit in our screen; Table S1), are epistatic in the repair of chemotherapy-induced DNA damage (Ward et al., 2017). Monoubiquitination of Fancd2 may recruit Pol θ to resected, RPA-coated ssDNA to promote alt-EJ between acentric DNA and its centric partner, which pulls acentric DNA into daughter nuclei (Fig. 7 G'). When Fancd2 monoubiquitination is disrupted and/or when *polQ* is knocked down, RPA-coated resected DNA persists, and the acentric detaches from centromere-containing chromosomes, causing micronuclei (Fig. 7, H and H').

In addition to *polQ*, our candidate screen can identify additional acentric DNA segregation mechanisms. We identified several structure-specific endonucleases (SSEs), which resolve replication and repair intermediates (Table S1; Minocherhomji and Hickson, 2014). It was recently identified that in *D. melanogaster*, *polQ* and the SSEs SLX4 and GEN1 process HR intermediates. *polQ* suppresses mitotic crossovers to prevent deleterious loss of heterozygosity (Carvajal-Garcia et al.,

2021). A similar *polQ*/SSE mechanism may also function in papillar cells.

Papillar cell acentric DNA segregation as a model for cancer cell biology and tumor resistance

We previously described characteristics of papillar cell biology that are similar to what is observed in cancer cells (Cohen et al., 2020; Peterson et al., 2020). Papillar cells are polyploid, as are more than one-third of cancers (Zack et al., 2013). Additionally, papillar cells resist multiple forms of DNA damage (Bretscher and Fox, 2016). Similarly, some cancer cells that undergo genome duplication also resist various DNA-damaging therapies, such as chemotherapy drugs or IR (Shen et al., 2008, 2013; Szakács et al., 2006). One potential mechanism for how cancer cells and papillar cells tolerate high levels of DNA damage may be a dysregulated DDR (Bretscher and Fox, 2016; Lord and Ashworth, 2012; Zheng et al., 2012). As highlighted here, our findings are also relevant to preventing micronuclei, a prominent cancer feature (Marcozzi et al., 2018). Micronuclei can lead to deleterious chromosome rearrangements (Crasta et al., 2012; Nazaryan-Petersen et al., 2020; Zhang et al., 2015; Liu et al., 2018; McLaughlin et al., 2020) and an inflammatory response linked to tumor formation and metastasis (Bakhomou et al., 2018; Harding et al., 2017; Mackenzie et al., 2017). Our studies here on Pol θ and Fancd2 add to the similarities between papillar cells and mechanisms that are relevant to cancer biology.

Materials and methods

D. melanogaster stocks

A detailed list of stocks used in this study is available in Table S2.

D. melanogaster culture and genetics

Flies were raised on standard fly food (Archon Scientific) at 22°C except for when experiments were conducted with *tub-Gal80^{ts}*. In experiments using *tub-Gal80^{ts}*, animals were raised at 18°C until the L2 stage, when DNA damage was induced (see DNA damage). Those animals were then shifted to 29°C during the feeding L3 stage.

The *fancd2*^{K595R/K595R} flies were generated by GenetiVision. The K595R mutation was created via two steps of CRISPR-Cas9-mediated homology-directed repair events. In the first step, two CRISPR-Cas9 targets were designed to delete a 490-bp fragment containing the K595. Two gRNAs were cloned into pCFD3 vector (http://www.flyrnai.org/tools/grna_tracker/web/files/Cloning-with-pCFD3.pdf), and a donor DNA was created with a GFP cassette flanked by two 1-kb *fancd2* sequences beyond cleavage sites. Upon coinjection of both DNA constructs, two

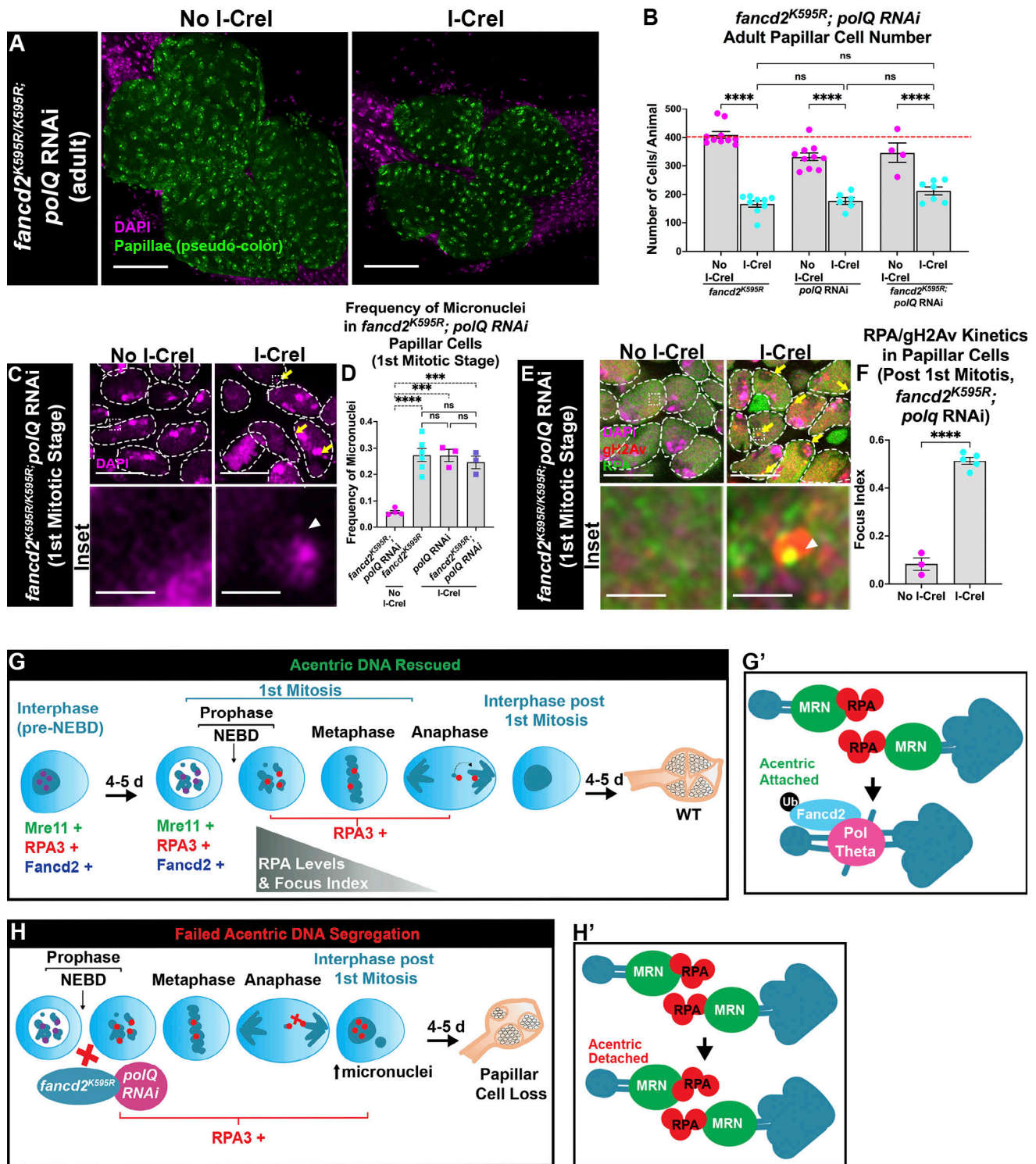


Figure 7. *polQ* and *fancd2* mutants are epistatic for micronuclei prevention during papillar cell mitosis. (A) Adult rectums of *fancd2*^{K595R}; *polQ* RNAi animals ± *hs-I-Crel*. Green, papillar cells (pseudocolored); magenta, DNA (DAPI). Scale bars = 50 μm. (B) Quantification of adult papillar cell number in *polQ* RNAi (dataset from Fig. 5 B), *fancd2*^{K595R} (dataset from Fig. 6 C), *fancd2*^{K595R}; *polQ* RNAi animals (+ *hs-I-Crel*, 1,487 cells, seven animals; - *hs-I-Crel*, 1,386 cells, four animals; P < 0.0001). Red dashed line indicates the expected number of papillar cells in a WT adult. Each condition represents two or more biological replicates. Each data point represents a single animal. Error bars indicate SEM. ****, P < 0.0001 by unpaired two-tailed t test without Welch's correlation. (C) Mitotic stage *fancd2*^{K595R}; *polQ* RNAi animals ± *hs-I-Crel*. Magenta, DNA (DAPI); yellow arrows, micronuclei; dashed box, area magnified ×10 in the corresponding inset; white arrowhead, enlarged micronucleus; dashed outline, nuclei. Scale bars = 10 μm; inset scale bar = 0.5 μm. (D) Quantification of the fate of acentric fragments in *fancd2*^{K595R}; *polQ* RNAi (+ *hs-I-Crel*, 107 cells, three animals; - *hs-I-Crel*, 272 cells, four animals; P < 0.0001), *fancd2*^{K595R} (dataset from Fig. 6 E), and *polQ* RNAi (dataset from Fig. 5 D) + *hs-I-Crel* papillar cells. Each time point represents two or more biological replicates. Each data point represents a single animal. Error bars indicate SEM. ***, P < 0.001; ****, P < 0.0001 by ordinary one-way ANOVA with Dunnett's multiple comparison test. (E) RPA and gH2Av

recruitment to *fancd2*^{K595R}; *polQ* RNAi papillar cells ± *hs-I-Crel*. Magenta, DNA (DAPI); green, RPA; red, gH2Av; yellow arrows, RPA⁺ gH2Av⁺ foci. All other labeling as in C. **(F)** Quantification of RPA⁺ gH2Av⁺ foci recruitment in *fancd2*^{K595R}; *polQ* RNAi papillar cells (+ *hs-I-Crel*, 153 cells, five animals; - *hs-I-Crel*, 113 cells, three animals) after the first mitotic stage. Each time point represents two or more biological replicates. Each data point represents a single animal. Error bars indicate SEM. ****, $P < 0.0001$ by ordinary one-way ANOVA with Dunnett's multiple comparison test. **(G-H)** Proposed model for how Pol θ and monoubiquitinated Fancd2 work in concert to promote acentric DNA segregation. Purple circles, Mre11⁺, RPA3⁺, and Fancd2⁺ foci; red circles, RPA3⁺ foci (see Discussion).

gRNAs were expressed to direct the DSB by Cas9 (endogenously expressed in the injection stock BL#54591). After the DSB, the GFP cassette was inserted into *fancd2* genome via donor DNA-mediated recombination. In the second step, based on the same principle, a 1,039-bp DNA-containing GFP cassette (plus neighboring *fancd2* sequences) was substituted by the mutant allele containing K595R using a new set of gRNAs and new donor DNA, which is the *fancd2* sequence with K595R mutation introduced.

The *Ubi-GFP-Fancd2* flies were generated by cloning full-length *D. melanogaster* Fancd2, fused to codon-optimized eGFP, and separated by a (GSSS)₄ linker at the N-terminus into a pBID vector (Addgene, Twist Bioscience). The resulting plasmid was used to make transgenic flies (Model System Injections, Duke University).

The stock containing *ry*⁷⁷⁶⁺ gRNA (ATTGTGGCGGAGATCTCG A) was made by the Sekelsky Laboratory at the University of North Carolina, Chapel Hill, Chapel Hill, NC. The gRNA was cloned into a pCFD3 vector (Phillip Port, Simon Bullock Laboratory, Medical Research Council Laboratory of Molecular Biology, Cambridge, UK) and injected at 58A using PhiC 31. The landing site has a 3×P3-DsRed marker, and the pCFD3 has a *vermillion*⁺ marker.

DNA damage

DSBs were induced using three methods. The first method uses animals expressing the *hs-I-Crel* transgene. DNA damage was induced using methods from [Bretscher and Fox \(2016\)](#) in which animals were heat shocked at 37°C for 90 min at the L2 stage. The second method to induce DSBs was using IR as described in [Bretscher and Fox \(2016\)](#) in which fly food containing L2 flies were placed in 60-mm Petri dishes. The Petri dishes were then placed in an X-RAD 160 PXI precision x-ray irradiator (calibrated by a dosimetrist) at 20 Gy. Lastly, DSBs were induced at the *ry* locus using CRISPR-Cas9 (see *D. melanogaster* culture and genetics). Animals expressing the *ry* gRNA were crossed to animals expressing *UAS-Cas9*; *byn-Gal4*, *tub-Gal80ts*. These animals were raised at 18°C until the L2 stage. Larvae were then shifted to 29°C for 24 h to allow for expression of Cas9 and subsequent induction of DSBs at the *ry* locus and then shifted back to 18°C.

Fixed imaging

D. melanogaster tissues were dissected in 1× PBS and immediately fixed in 3.7% formaldehyde + 0.3% Triton-X. Immunofluorescence staining was performed as in [Sawyer et al. \(2017\)](#) in which fixed tissues were washed with 1× PBS three times and then blocked with 1× PBS, 0.3% Triton X-100, and 1% normal goat serum. Tissues were then incubated in primary antibodies diluted in block solution at 4°C overnight. Primary antibodies were washed out three times with 1× PBS, and then tissue was incubated in block solution with DAPI at 5 µg/ml. Tissue was then incubated in secondary antibody at RT for 2 h. Secondary

antibodies were washed out three times with 1× PBS. Tissues were mounted in VECTASHIELD (Vector Laboratories). Primary antibodies used in this study were mouse anti-gamma H2Av (1:2,500, UNC93-5.2.1; Developmental Studies Hybridoma Bank), rabbit anti-GFP (1:1,000, A-11122; Thermo Fisher Scientific), rabbit anti-Rad51 (1:500; a gift from James Kadonaga, University of California, San Diego), and rabbit anti-RPA (1:1,000, a gift from J. Nordman, Vanderbilt University, Nashville, TN, generated by P. Fisher, Stony Brook University, Stony Brook, NY). Secondary antibodies used were goat anti-rabbit Alexa Fluor 488 (1:500, A-11008; Invitrogen) and goat anti-mouse Alexa Fluor 568 (1:500, A-11004; Invitrogen).

All fixed images presented in the figures were acquired using a Zeiss 880 Airyscan Inverted Confocal Microscope using a Plan-Aprochromat 20×/0.80 NA air objective (420650-9901) and Plan-Aprochromat 63×/1.4 NA oil objective (420782-9900). 405-nm diode, argon/2 488, and 561-nm diode lasers were used on a Zeiss Axio Observer Z1 with Definite Focus 2. The system was controlled by Zen 2.3 software (Zeiss). Airyscan processing was performed on all images after acquisition. Adult rectum images were acquired using Zeiss Axio Imager M2 with Apotome processing using an EC Plan-Neofluar 20×/0.5 NA air objective. Additional imaging for quantitation only was performed using an Andor Dragonfly 505 unit with Borealis illumination spinning disk confocal microscope with Andor iXon Life 888 1,024 × 1,024 EMCCD camera and an HC PL APO 63×/1.47 CORR TIRF (11506319; Leica) oil objective (405 nm [100 mW], 488 nm [150 mW], and 561 nm [100 mW] diodes) on a Leica DMi8 microscope. The system was controlled by Fusion software. All images were acquired at RT.

Live imaging

Tissues were prepared for live imaging as described in previous studies ([Fox et al., 2010](#); [Schoenfelder et al., 2014](#)). Tissues were dissected in Schneider's *Drosophila* medium (11720-034; Invitrogen) with 15% vol/vol FBS, 0.6× penicillin/streptomycin, and 0.2 mg/ml insulin. Tissues were mounted on a flexible membrane with Halocarbon 27 Oil (H8773; Sigma) under a coverslip. Images were acquired on a spinning disk confocal microscope (CSU10 scanhead; Yokogawa Electric Corporation) on an Olympus IX70 inverted microscope using a UPlanSApo 60×/1.3 NA silicon oil objective, 488- and 568-nm Kr-Ar laser lines for excitation, and an Andor iXon 3 897 512 EMCCD camera. The system was controlled by MetaMorph 7.7 software. All images were acquired at RT.

Image analysis

All image analyses were performed using ImageJ software ([Schneider et al., 2012](#)). Adult papillae were pseudocolored as

done previously (Schoenfelder et al., 2014, Bretscher and Fox, 2016; Stormo and Fox, 2016, 2019; Peterson et al., 2020). Focus index was determined as the percentage of cells with at least one DNA repair focus. Individual foci were not counted due to somatic chromosome pairing in which foci in these cells can coalesce into a single focus. Mre11-GFP foci in fixed tissues were not as distinguishable as RPA3-GFP foci and thus were determined using colocalization with gH2AV antibody. Focus index, micronuclei frequency, and adult papillar cell number were quantified using ImageJ Cell Counter plugin. Foci intensity was calculated by measuring mean fluorescence intensity of individual foci. Images were converted to grayscale, and individual regions of interest (ROIs) were drawn around multiple foci within each cell across different stages of cell division (interphase, prophase [before and after NEBD], metaphase, anaphase, and interphase following the first division). Measurements of individual ROIs were taken using the mean gray value. ROIs of the same size were taken from background on the same stack and time point as the relevant foci, and mean intensity values were averaged and subtracted from each focus mean intensity value.

Statistics

All statistics were computed in Prism 8 and 9 (GraphPad Software). Adult papillar cell number and micronuclei frequency for animals expressing various RNAi constructs were analyzed using unpaired two-tailed *t* test without Welch's correlation (no DNA damage vs. DNA damage). Focus index, fluorescence intensity measurements, and any other comparisons of three or more groups were analyzed using ordinary one-way ANOVA with Dunnett's multiple comparison test (data points compared with no DNA damage control). *P* values and cell numbers are indicated in figure legends. Data distribution was assumed to be normal, but this was not formally tested. Statistical notations used in figures include *, $P \leq 0.05$; **, $P \leq 0.01$; ***, $P \leq 0.001$; ****, $P \leq 0.0001$.

Online supplemental material

Fig. S1 shows that Mre11 and RPA are recruited to papillar cells with delayed kinetics after IR-induced DSBs. Fig. S2 shows that Rad51 is not required for cell survival following DSBs in papillar cells. Fig. S3 shows that FA proteins are required for proper RPA3+ foci dynamics and cell survival following DSBs. Table S1 lists results from a candidate screen for regulators of acentric DNA segregation during mitosis in papillar cells. Table S2 lists all the fly stocks used in this study.

Acknowledgments

We thank the Bloomington Drosophila Stock Center, Developmental Studies Hybridoma Bank, and Vienna Drosophila Resource Center for providing the reagents used in this study. We thank Dr. Fu Yang and Dr. Zhao Zhang for comments on the manuscript and Dr. Lisa Cameron and Dr. Yasheng Gao (Duke Light Microscopy Core Facility) for assistance.

This project was supported by National Institute of General Medical Sciences grant GM118447 to D.T. Fox, a National Science Foundation Graduate Research Fellowship Program grant to D.E.

Clay, and National Cancer Institute grant F31CA186545 to H.S. Bretscher.

The authors declare no competing financial interests.

Author contributions: Conceptualization: D.E. Clay, H.S. Bretscher, and D.T. Fox. Methodology: D.E. Clay, H.S. Bretscher, E.A. Jezuit, and K.B. Bush. Validation: D.E. Clay, H.S. Bretscher, E.A. Jezuit, and K.B. Bush. Formal analysis: D.E. Clay, H.S. Bretscher, E.A. Jezuit, K.B. Bush, and D.T. Fox. Investigation: D.E. Clay, H.S. Bretscher, E.A. Jezuit, and K.B. Bush. Data curation: D.E. Clay, H.S. Bretscher, E.A. Jezuit, and K.B. Bush. Writing: D.E. Clay and D.T. Fox. Visualization: D.E. Clay, H.S. Bretscher, and E.A. Jezuit. Supervision: D.T. Fox. Funding acquisition: D.E. Clay, H.S. Bretscher, and D.T. Fox.

Submitted: 18 June 2021

Revised: 24 August 2021

Accepted: 14 September 2021

References

- Ahmad, A., A.R. Robinson, A. Duensing, E. van Drunen, H.B. Beverloo, D.B. Weisberg, P. Hasty, J.H.J. Hoeijmakers, and L.J. Niedernhofer. 2008. ERCC1-XPF endonuclease facilitates DNA double-strand break repair. *Mol. Cell. Biol.* 28:5082–5092. <https://doi.org/10.1128/MCB.00293-08>
- Aleksandrov, R., R. Hristova, S. Stoyanov, and A. Gospodinov. 2020. The chromatin response to double-strand DNA breaks and their repair. *Cells*. 9:1853. <https://doi.org/10.3390/cells9081853>
- Bakhoun, S.F., B. Ngo, A.M. Laughney, J.-A. Cavallo, C.J. Murphy, P. Ly, P. Shah, R.K. Sriram, T.B.K. Watkins, N.K. Taunk, et al. 2018. Chromosomal instability drives metastasis through a cytosolic DNA response. *Nature*. 553:467–472. <https://doi.org/10.1038/nature25432>
- Beagan, K., and M. McVey. 2016. Linking DNA polymerase theta structure and function in health and disease. *Cell. Mol. Life Sci.* 73:603–615. <https://doi.org/10.1007/s00018-015-2078-9>
- Beagan, K., R.L. Armstrong, A. Witsell, U. Roy, N. Renedo, A.E. Baker, O.D. Schärer, and M. McVey. 2017. Drosophila DNA polymerase theta utilizes both helicase-like and polymerase domains during microhomology-mediated end joining and interstrand crosslink repair. *PLoS Genet.* 13:e1006813. <https://doi.org/10.1371/journal.pgen.1006813>
- Bretscher, H.S., and D.T. Fox. 2016. Proliferation of double-strand break-resistant polyploid cells requires Drosophila FANCD2. *Dev. Cell.* 37:444–457. <https://doi.org/10.1016/j.devcel.2016.05.004>
- Calvi, B.R. 2013. Making big cells: One size does not fit all. *Proc. Natl. Acad. Sci. USA.* 110:9621–9622. <https://doi.org/10.1073/pnas.1306908110>
- Cannan, W.J., and D.S. Pederson. 2016. Mechanisms and consequences of double-strand DNA break formation in chromatin. *J. Cell. Physiol.* 231:3–14. <https://doi.org/10.1002/jcp.25048>
- Carvajal-Garcia, J., K.N. Crown, D.A. Ramsden, and J. Sekelsky. 2021. DNA polymerase theta suppresses mitotic crossing over. *PLoS Genet.* 17:e1009267. <https://doi.org/10.1371/journal.pgen.1009267>
- Ceccaldi, R., J.C. Liu, R. Amunugama, I. Hajdu, B. Primack, M.I. Petalcorin, K.W. O'Connor, P.A. Konstantinopoulos, S.J. Elledge, S.J. Boulton, et al. 2015. Homologous-recombination-deficient tumours are dependent on Polθ-mediated repair. *Nature*. 518:258–262. <https://doi.org/10.1038/nature14184>
- Ceccaldi, R., B. Rondinelli, and A.D. D'Andrea. 2016. Repair pathway choices and consequences at the double-strand break. *Trends Cell Biol.* 26:52–64. <https://doi.org/10.1016/j.tcb.2015.07.009>
- Chan, S.H., A.M. Yu, and M. McVey. 2010. Dual roles for DNA polymerase theta in alternative end-joining repair of double-strand breaks in Drosophila. *PLoS Genet.* 6:e1001005. <https://doi.org/10.1371/journal.pgen.1001005>
- Chang, H.H.Y., N.R. Pannunzio, N. Adachi, and M.R. Lieber. 2017. Non-homologous DNA end joining and alternative pathways to double-strand break repair. *Nat. Rev. Mol. Cell Biol.* 18:495–506. <https://doi.org/10.1038/nrm.2017.48>
- Chiolo, I., A. Minoda, S.U. Colmenares, A. Polyzos, S.V. Costes, and G.H. Karpen. 2011. Double-strand breaks in heterochromatin move outside

- of a dynamic HPIa domain to complete recombinational repair. *Cell*. 144: 732–744. <https://doi.org/10.1016/j.cell.2011.02.012>
- Ciccia, A., and S.J. Elledge. 2010. The DNA damage response: Making it safe to play with knives. *Mol. Cell*. 40:179–204. <https://doi.org/10.1016/j.molcel.2010.09.019>
- Cohen, E., J.K. Sawyer, N.G. Peterson, J.A.T. Dow, and D.T. Fox. 2020. Physiology, development, and disease modeling in the *Drosophila* excretory system. *Genetics*. 214:235–264. <https://doi.org/10.1534/genetics.119.302289>
- Crasta, K., N.J. Ganem, R. Dagher, A.B. Lantermann, E.V. Ivanova, Y. Pan, L. Nezi, A. Protopopov, D. Chowdhury, and D. Pellman. 2012. DNA breaks and chromosome pulverization from errors in mitosis. *Nature*. 482: 53–58. <https://doi.org/10.1038/nature10802>
- Deng, L., R.A. Wu, R. Sonnevile, O.V. Kochenova, K. Labib, D. Pellman, and J.C. Walter. 2019. Mitotic CDK promotes replisome disassembly, fork breakage, and complex DNA rearrangements. *Mol. Cell*. 73:915–929.e6. <https://doi.org/10.1016/j.molcel.2018.12.021>
- Derive, N., C. Landmann, E. Montembault, M.-C. Claverie, P. Pierre-Elies, D. Goutte-Gattat, N. Founounou, D. McCusker, and A. Royou. 2015. Bub3-BubR1-dependent sequestration of Cdc20Fizzy at DNA breaks facilitates the correct segregation of broken chromosomes. *J. Cell Biol.* 211:517–532. <https://doi.org/10.1083/jcb.201504059>
- Dialynas, G., L. Delabaere, and I. Chiolo. 2019. Arp2/3 and Unc45 maintain heterochromatin stability in *Drosophila* polytene chromosomes. *Exp. Biol. Med.* (Maywood). 244:1362–1371. <https://doi.org/10.1177/1535370219862282>
- Dumont, J., K. Oegema, and A. Desai. 2010. A kinetochore-independent mechanism drives anaphase chromosome separation during acentrosomal meiosis. *Nat. Cell Biol.* 12:894–901. <https://doi.org/10.1038/ncb2093>
- Durante, M., and S.C. Formenti. 2018. Radiation-induced chromosomal aberrations and immunotherapy: Micronuclei, cytosolic DNA, and interferon-production pathway. *Front. Oncol.* 8:192. <https://doi.org/10.3389/fonc.2018.00192>
- Fernandez-Vidal, A., L. Guitton-Sert, J.-C. Cadoret, M. Drac, E. Schwob, G. Baldacci, C. Cazaux, and J.-S. Hoffmann. 2014. A role for DNA polymerase θ in the timing of DNA replication. *Nat. Commun.* 5:4285. <https://doi.org/10.1038/ncomms5285>
- Finn, K., N.F. Lowndes, and M. Grenon. 2012. Eukaryotic DNA damage checkpoint activation in response to double-strand breaks. *Cell. Mol. Life Sci.* 69:1447–1473. <https://doi.org/10.1007/s00018-011-0875-3>
- Fox, D.T., and R.J. Duronio. 2013. Endoreplication and polyploidy: Insights into development and disease. *Development*. 140:3–12. <https://doi.org/10.1242/dev.080531>
- Fox, D.T., J.G. Gall, and A.C. Spradling. 2010. Error-prone polyploid mitosis during normal *Drosophila* development. *Genes Dev.* 24:2294–2302. <https://doi.org/10.1101/gad.1952710>
- Furuta, T., H. Takemura, Z.-Y. Liao, G.J. Aune, C. Redon, O.A. Sedelnikova, D.R. Pilch, E.P. Rogakou, A. Celeste, H.T. Chen, et al. 2003. Phosphorylation of histone H2AX and activation of Mre11, Rad50, and Nbs1 in response to replication-dependent DNA double-strand breaks induced by mammalian DNA topoisomerase I cleavage complexes. *J. Biol. Chem.* 278:20303–20312. <https://doi.org/10.1074/jbc.M300198200>
- Hafner, A., M.L. Bulyk, A. Jambhekar, and G. Lahav. 2019. The multiple mechanisms that regulate p53 activity and cell fate. *Nat. Rev. Mol. Cell Biol.* 20:199–210. <https://doi.org/10.1038/s41580-019-0110-x>
- Hanscom, T., and M. McVey. 2020. Regulation of error-prone DNA double-strand break repair and its impact on genome evolution. *Cells*. 9:1657. <https://doi.org/10.3390/cells9071657>
- Harding, S.M., J.L. Benci, J. Irianto, D.E. Discher, A.J. Minn, and R.A. Greenberg. 2017. Mitotic progression following DNA damage enables pattern recognition within micronuclei. *Nature*. 548:466–470. <https://doi.org/10.1038/nature23470>
- Harper, J.W., and S.J. Elledge. 2007. The DNA damage response: Ten years after. *Mol. Cell*. 28:739–745. <https://doi.org/10.1016/j.molcel.2007.11.015>
- Hassel, C., B. Zhang, M. Dixon, and B.R. Calvi. 2014. Induction of endocycles represses apoptosis independently of differentiation and predisposes cells to genome instability. *Development*. 141:112–123. <https://doi.org/10.1242/dev.098871>
- Iliakis, G., T. Murmann, and A. Soni. 2015. Alternative end-joining repair pathways are the ultimate backup for abrogated classical non-homologous end-joining and homologous recombination repair: Implications for the formation of chromosome translocations. *Mutat. Res. Genet. Toxicol. Environ. Mutagen.* 793:166–175. <https://doi.org/10.1016/j.mrgentox.2015.07.001>
- Ishii, K., Y. Ogiyama, Y. Chikashige, S. Soejima, F. Masuda, T. Kakuma, Y. Hiraoka, and K. Takahashi. 2008. Heterochromatin integrity affects chromosome reorganization after centromere dysfunction. *Science*. 321: 1088–1091. <https://doi.org/10.1126/science.1158699>
- Iwaki, D.D., and J.A. Lengyel. 2002. A Delta-Notch signaling border regulated by Engrailed/Invected repression specifies boundary cells in the *Drosophila* hindgut. *Mech. Dev.* 114:71–84. [https://doi.org/10.1016/S0925-4773\(02\)00061-8](https://doi.org/10.1016/S0925-4773(02)00061-8)
- Jackson, S.P., and J. Bartek. 2009. The DNA-damage response in human biology and disease. *Nature*. 461:1071–1078. <https://doi.org/10.1038/nature08467>
- Jaklevic, B., L. Uyetake, W. Lemstra, J. Chang, W. Leary, A. Edwards, S. Vidwans, O. Sibon, and T. Tin Su. 2006. Contribution of growth and cell cycle checkpoints to radiation survival in *Drosophila*. *Genetics*. 174: 1963–1972. <https://doi.org/10.1534/genetics.106.064477>
- Kais, Z., B. Rondinelli, A. Holmes, C. O’Leary, D. Kozono, A.D. D’Andrea, and R. Ceccaldi. 2016. FANCD2 maintains fork stability in BRCA1/2-deficient tumors and promotes alternative end-joining DNA repair. *Cell Rep.* 15: 2488–2499. <https://doi.org/10.1016/j.celrep.2016.05.031>
- Karg, T., B. Warecki, and W. Sullivan. 2015. Aurora B-mediated localized delays in nuclear envelope formation facilitate inclusion of late-segregating chromosome fragments. *Mol. Biol. Cell*. 26:2227–2241. <https://doi.org/10.1091/mbc.E15-01-0026>
- Karg, T., M.W. Elting, H. Vicars, S. Dumont, and W. Sullivan. 2017. The chromokinesin Klp3a and microtubules facilitate acentric chromosome segregation. *J. Cell Biol.* 216:1597–1608. <https://doi.org/10.1083/jcb.201604079>
- Kent, T., G. Chandramouly, S.M. McDevitt, A.Y. Ozdemir, and R.T. Pomerantz. 2015. Mechanism of microhomology-mediated end-joining promoted by human DNA polymerase θ . *Nat. Struct. Mol. Biol.* 22:230–237. <https://doi.org/10.1038/nsmb.2961>
- Kondo, S., and N. Perrimon. 2011. A genome-wide RNAi screen identifies core components of the G₂-M DNA damage checkpoint. *Sci. Signal.* 4:rs1. <https://doi.org/10.1126/scisignal.2001350>
- Landmann, C., P. Pierre-Elies, D. Goutte-Gattat, E. Montembault, M.C. Claverie, and A. Royou. 2020. The Mre11-Rad50-Nbs1 complex mediates the robust recruitment of Polo to DNA lesions during mitosis in *Drosophila*. *J. Cell Sci.* 133:jcs244442.
- Liang, L., L. Deng, Y. Chen, G.C. Li, C. Shao, and J.A. Tischfield. 2005. Modulation of DNA end joining by nuclear proteins. *J. Biol. Chem.* 280: 31442–31449. <https://doi.org/10.1074/jbc.M503776200>
- Liu, Y., C.F. Nielsen, Q. Yao, and I.D. Hickson. 2014. The origins and processing of ultra fine anaphase DNA bridges. *Curr. Opin. Genet. Dev.* 26: 1–5. <https://doi.org/10.1016/j.gde.2014.03.003>
- Liu, H., H. Zhang, X. Wu, D. Ma, J. Wu, L. Wang, Y. Jiang, Y. Fei, C. Zhu, R. Tan, et al. 2018. Nuclear cGAS suppresses DNA repair and promotes tumorigenesis. *Nature*. 563:131–136. <https://doi.org/10.1038/s41586-018-0629-6>
- Lord, C.J., and A. Ashworth. 2012. The DNA damage response and cancer therapy. *Nature*. 481:287–294. <https://doi.org/10.1038/nature10760>
- Ma, J.-L., E.M. Kim, J.E. Haber, and S.E. Lee. 2003. Yeast Mre11 and Rad1 proteins define a Ku-independent mechanism to repair double-strand breaks lacking overlapping end sequences. *Mol. Cell Biol.* 23:8820–8828. <https://doi.org/10.1128/MCB.23.23.8820-8828.2003>
- Mackenzie, K.J., P. Carroll, C.-A. Martin, O. Murina, A. Fluteau, D.J. Simpson, N. Olova, H. Sutcliffe, J.K. Rainger, A. Leitch, et al. 2017. cGAS surveillance of micronuclei links genome instability to innate immunity. *Nature*. 548:461–465. <https://doi.org/10.1038/nature23449>
- Marcozzi, A., F. Pellestor, and W.P. Kloosterman. 2018. The genomic characteristics and origin of chromothripsis. *Methods Mol. Biol.* 1769:3–19. https://doi.org/10.1007/978-1-4939-7780-2_1
- Marek, L.R., and A.E. Bale. 2006. *Drosophila* homologs of FANCD2 and FANCL function in DNA repair. *DNA Repair (Amst.)*. 5:1317–1326. <https://doi.org/10.1016/j.dnarep.2006.05.044>
- McLaughlin, M., E.C. Patin, M. Pedersen, A. Wilkins, M.T. Dillon, A.A. Melcher, and K.J. Harrington. 2020. Inflammatory microenvironment remodelling by tumour cells after radiotherapy. *Nat. Rev. Cancer*. 20: 203–217. <https://doi.org/10.1038/s41568-020-0246-1>
- McVey, M., and S.E. Lee. 2008. MMEJ repair of double-strand breaks (director’s cut): Deleted sequences and alternative endings. *Trends Genet.* 24:529–538. <https://doi.org/10.1016/j.tig.2008.08.007>
- Mehrotra, S., S.B. Maqbool, A. Kolpakas, K. Murnen, and B.R. Calvi. 2008. Endocycling cells do not apoptose in response to DNA rereplication genotoxic stress. *Genes Dev.* 22:3158–3171. <https://doi.org/10.1101/gad.1710208>

- Minocherhomji, S., and I.D. Hickson. 2014. Structure-specific endonucleases: guardians of fragile site stability. *Trends Cell Biol.* 24:321–327. <https://doi.org/10.1016/j.tcb.2013.11.007>
- Murcia, L., M. Clemente-Ruiz, P. Pierre-Elies, A. Royou, and M. Milán. 2019. Selective killing of RAS-malignant tissues by exploiting oncogene-induced DNA damage. *Cell Rep.* 28:119–131.e4. <https://doi.org/10.1016/j.celrep.2019.06.004>
- Muzzini, D.M., P. Plevani, S.J. Boulton, G. Cassata, and F. Marini. 2008. Caenorhabditis elegans POLQ-1 and HEL-308 function in two distinct DNA interstrand cross-link repair pathways. *DNA Repair (Amst.)* 7: 941–950. <https://doi.org/10.1016/j.dnarep.2008.03.021>
- Nakamura, K., T. Kogame, H. Oshiumi, A. Shinohara, Y. Sumitomo, K. Agama, Y. Pommier, K.M. Tsutsui, K. Tsutsui, E. Hartsuiker, et al. 2010. Collaborative action of Brc1 and CtIP in elimination of covalent modifications from double-strand breaks to facilitate subsequent break repair. *PLoS Genet.* 6: e1000828. <https://doi.org/10.1371/journal.pgen.1000828>
- Nazaryan-Petersen, L., V.A. Bjerregaard, F.C. Nielsen, N. Tommerup, and Z. Tümer. 2020. Chromothripsis and DNA repair disorders. *J. Clin. Med.* 9: 613. <https://doi.org/10.3390/jcm9030613>
- Ohno, Y., Y. Ogiyama, Y. Kubota, T. Kubo, and K. Ishii. 2016. Acentric chromosome ends are prone to fusion with functional chromosome ends through a homology-directed rearrangement. *Nucleic Acids Res.* 44: 232–244. <https://doi.org/10.1093/nar/gkv997>
- Øvrebo, J.I., and B.A. Edgar. 2018. Polyploidy in tissue homeostasis and regeneration. *Development.* 145:dev156034. <https://doi.org/10.1242/dev.156034>
- Peterson, C., G.E. Carney, B.J. Taylor, and K. White. 2002. Reaper is required for neuroblast apoptosis during Drosophila development. *Development.* 129:1467–1476. <https://doi.org/10.1242/dev.129.6.1467>
- Peterson, N.G., B.M. Stormo, K.P. Schoenfelder, J.S. King, R.R.S. Lee, and D.T. Fox. 2020. Cytoplasmic sharing through apical membrane remodeling. *eLife.* 9:e58107. <https://doi.org/10.7554/eLife.58107>
- Petsalaki, E., and G. Zachos. 2020. DNA damage response proteins regulating mitotic cell division: Double agents preserving genome stability. *FEBS J.* 287:1700–1721. <https://doi.org/10.1111/febs.15240>
- Rodríguez, A., and A. D'Andrea. 2017. Fanconi anemia pathway. *Curr. Biol.* 27: R986. <https://doi.org/10.1016/j.cub.2017.07.043>
- Rong, Y.S., S.W. Titen, H.B. Xie, M.M. Golic, M. Bastiani, P. Bandyopadhyay, B.M. Olivera, M. Brodsky, G.M. Rubin, and K.G. Golic. 2002. Targeted mutagenesis by homologous recombination in *D. melanogaster*. *Genes Dev.* 16:1568–1581. <https://doi.org/10.1101/gad.986602>
- Royou, A., H. Macias, and W. Sullivan. 2005. The Drosophila Grp/Chk1 DNA damage checkpoint controls entry into anaphase. *Curr. Biol.* 15:334–339. <https://doi.org/10.1016/j.cub.2005.02.026>
- Royou, A., M.E. Gagou, R. Karess, and W. Sullivan. 2010. BubR1- and Polo-coated DNA tethers facilitate poleward segregation of acentric chromatids. *Cell.* 140:235–245. <https://doi.org/10.1016/j.cell.2009.12.043>
- Santivasi, W.L., and F. Xia. 2014. Ionizing radiation-induced DNA damage, response, and repair. *Antioxid. Redox Signal.* 21:251–259. <https://doi.org/10.1089/ars.2013.5668>
- Sawyer, J., E. Cohen, and D. Fox. 2017. Interorgan regulation of *Drosophila* intestinal stem cell proliferation by a hybrid organ boundary zone. *Development.* 144:4091–4102.
- Schneider, C.A., W.S. Rasband, and K.W. Eliceiri. 2012. NIH Image to ImageJ: 25 years of image analysis. *Nat. Methods.* 9:671–675. <https://doi.org/10.1038/nmeth.2089>
- Schoenfelder, K.P., R.A. Montague, S.V. Paramore, A.L. Lennox, A.P. Mahowald, and D.T. Fox. 2014. Indispensable pre-mitotic endocycles promote aneuploidy in the *Drosophila* rectum. *Development.* 141:3551–3560. <https://doi.org/10.1242/dev.109850>
- Sekelsky, J. 2017. DNA repair in *Drosophila*: Mutagens, models, and missing genes. *Genetics.* 205:471–490. <https://doi.org/10.1534/genetics.116.186759>
- Sharma, S., S.M. Javadekar, M. Pandey, M. Srivastava, R. Kumari, and S.C. Raghavan. 2015. Homology and enzymatic requirements of microhomology-dependent alternative end joining. *Cell Death Dis.* 6:e1697. <https://doi.org/10.1038/cddis.2015.58>
- Shen, H., D.M. Moran, and C.G. Maki. 2008. Transient nutlin-3a treatment promotes endoreduplication and the generation of therapy-resistant tetraploid cells. *Cancer Res.* 68:8260–8268. <https://doi.org/10.1158/0008-5472.CAN-08-1901>
- Shen, H., R.E. Perez, B. Davaadelger, and C.G. Maki. 2013. Two 4N cell-cycle arrests contribute to cisplatin-resistance. *PLoS One.* 8:e59848. <https://doi.org/10.1371/journal.pone.0059848>
- Stormo, B.M., and D.T. Fox. 2016. Distinct responses to reduplicated chromosomes require distinct Mad2 responses. *eLife.* 5:e15204. <https://doi.org/10.7554/eLife.15204>
- Stormo, B.M., and D.T. Fox. 2019. Interphase cohesin regulation ensures mitotic fidelity after genome reduplication. *Mol. Biol. Cell.* 30:219–227. <https://doi.org/10.1091/mbc.E17-10-0582>
- Syed, A., and J.A. Tainer. 2018. The MRE11-RAD50-NBS1 complex conducts the orchestration of damage signaling and outcomes to stress in DNA replication and repair. *Annu. Rev. Biochem.* 87:263–294. <https://doi.org/10.1146/annurev-biochem-062917-012415>
- Szakács, G., J.K. Paterson, J.A. Ludwig, C. Booth-Genthe, and M.M. Gottesman. 2006. Targeting multidrug resistance in cancer. *Nat. Rev. Drug Discov.* 5:219–234. <https://doi.org/10.1038/nrd1984>
- Thyme, S.B., and A.F. Schier. 2016. Polq-mediated end joining is essential for surviving DNA double-strand breaks during early zebrafish development. *Cell Rep.* 15:707–714. <https://doi.org/10.1016/j.celrep.2016.03.072>
- Tisi, R., J. Vertemara, G. Zampella, and M.P. Longhese. 2020. Functional and structural insights into the MRX/MRN complex, a key player in recognition and repair of DNA double-strand breaks. *Comput. Struct. Biotechnol. J.* 18:1137–1152. <https://doi.org/10.1016/j.csbj.2020.05.013>
- Vignard, J., G. Mirey, and B. Salles. 2013. Ionizing-radiation induced DNA double-strand breaks: a direct and indirect lighting up. *Radiother. Oncol.* 108:362–369. <https://doi.org/10.1016/j.radonc.2013.06.013>
- Ward, T.A., P.J. McHugh, and S.T. Durant. 2017. Small molecule inhibitors uncover synthetic genetic interactions of human flap endonuclease 1 (FEN1) with DNA damage response genes. *PLoS One.* 12:e0179278. <https://doi.org/10.1371/journal.pone.0179278>
- Warecki, B., and W. Sullivan. 2020. Mechanisms driving acentric chromosome transmission. *Chromosome Res.* 28:229–246. <https://doi.org/10.1007/s10577-020-09636-z>
- Warecki, B., X. Ling, I. Bast, and W. Sullivan. 2020. ESCRT-III-mediated membrane fusion drives chromosome fragments through nuclear envelope channels. *J. Cell Biol.* 219:e201905091. <https://doi.org/10.1083/jcb.201905091>
- Wood, R.D., and S. Doublé. 2016. DNA polymerase θ (POLQ), double-strand break repair, and cancer. *DNA Repair (Amst.)* 44:22–32. <https://doi.org/10.1016/j.dnarep.2016.05.003>
- Wright, W.D., S.S. Shah, and W.D. Heyer. 2018. Homologous recombination and the repair of DNA double-strand breaks. *J. Biol. Chem.* 293: 10524–10535. <https://doi.org/10.1074/jbc.TM118.000372>
- Yang, H., S. Ren, S. Yu, H. Pan, T. Li, S. Ge, J. Zhang, and N. Xia. 2020. Methods favoring homology-directed repair choice in response to CRISPR/Cas9 induced-double strand breaks. *Int. J. Mol. Sci.* 21:6461. <https://doi.org/10.3390/ijms21186461>
- Zack, T.I., S.E. Schumacher, S.L. Carter, A.D. Cherniack, G. Saksena, B. Tabak, M.S. Lawrence, C.Z. Zhang, J. Wala, C.H. Mermel, et al. 2013. Pan-cancer patterns of somatic copy number alteration. *Nat. Genet.* 45: 1134–1140. <https://doi.org/10.1038/ng.2760>
- Zhang, C.-Z., A. Spektor, H. Cornils, J.M. Francis, E.K. Jackson, S. Liu, M. Meyerson, and D. Pellman. 2015. Chromothripsis from DNA damage in micronuclei. *Nature.* 522:179–184. <https://doi.org/10.1038/nature14493>
- Zheng, L., H. Dai, M. Zhou, X. Li, C. Liu, Z. Guo, X. Wu, J. Wu, C. Wang, J. Zhong, et al. 2012. Polyploid cells rewire DNA damage response networks to overcome replication stress-induced barriers for tumour progression. *Nat. Commun.* 3:815. <https://doi.org/10.1038/ncomms1825>

Supplemental material

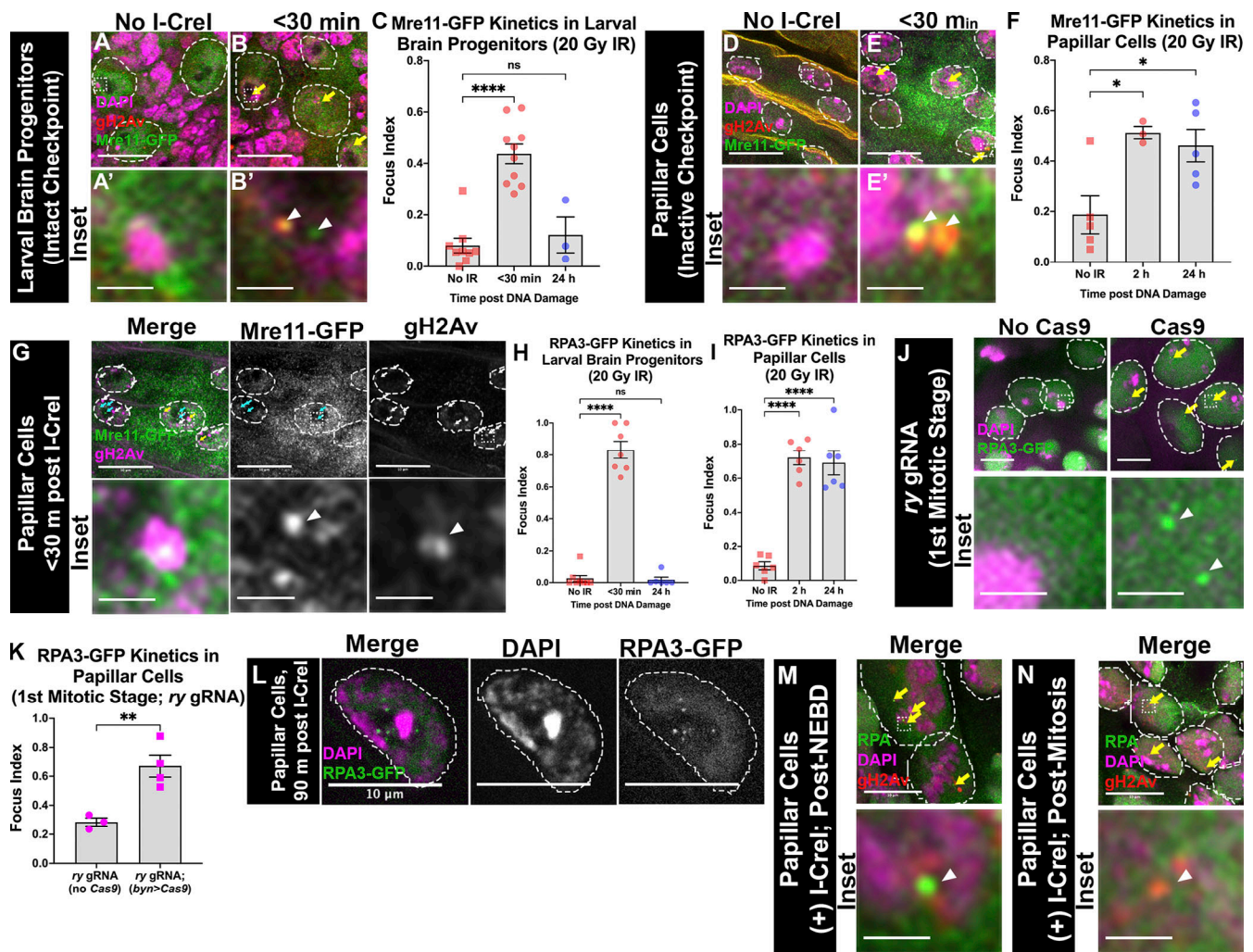


Figure S1. **Mre11 and RPA are recruited to papillar cells with delayed kinetics after IR-induced DSBs.** (A–B') Mre11-GFP colocalization with gH2Av in larval brain progenitors <30 min after \pm *hs-I-Crel*. Green, Mre11-GFP; magenta, DAPI (DNA); red, gH2Av; yellow arrow, Mre11⁺ foci; dashed outlines, nuclei; dashed box, area magnified $\times 10$ in the corresponding inset; white arrowheads, enlarged foci. Scale bars = 10 μ m; inset scale bar = 0.5 μ m. (C) Mre11-GFP localization over time in larval brain progenitors \pm IR (No IR, 106 cells, 9 animals; <30 min, 813 cells, 10 animals; 24 h, 1,185 cells, 3 animals). Each time point represents two or more biological replicates. Each data point represents a single animal. Error bars indicate SEM. ****, $P < 0.0001$ by ordinary one-way ANOVA with Dunnett's multiple comparison test. (D–E') Mre11-GFP colocalization with gH2Av in papillar cells <30 min after \pm *hs-I-Crel*. Labeling as in A–B'. (F) Mre11-GFP localization over time in papillar cells \pm IR (No IR, 383 cells, five animals; 2 h, 197 cells, three animals; 24 h, 321 cells, five animals; $P = 0.0147$). Each time point represents two or more biological replicates. Each data point represents a single animal. Error bars indicate SEM. *, $P < 0.05$ by ordinary one-way ANOVA with Dunnett's multiple comparison test. (G) Mre11⁺ gH2Av⁺ (yellow arrows), Mre11⁺ (cyan arrows), and gH2Av⁺ (white arrows) foci in papillar cells <30 min after \pm *hs-I-Crel*. Labeling as in A–B' except for the following: green, Mre11; magenta, gH2Av. (H) RPA3-GFP localization over time in larval brain progenitors \pm IR (No IR, 80 cells, eight animals; <30 min, 17 cells, seven animals; 24 h, 34 cells, six animals; $P < 0.0001$). (I) RPA3-GFP localization over time in papillar cells \pm IR (No IR, 90 cells, six animals; 2 h, 338 cells, six animals; 24 h, 81 cells, six animals; $P < 0.0001$). Each time point represents two or more biological replicates. Each data point represents a single animal. Error bars indicate SEM. ****, $P < 0.0001$ by ordinary one-way ANOVA with Dunnett's multiple comparison test. (J) RPA3 recruitment to papillar cells \pm Cas9-induced DSBs using *ry* gRNA. RPA3⁺ foci are marked with yellow arrows. Labeling as in A–B' except for the following: magenta, DAPI (DNA); green, RPA3. (K) Quantification of RPA3-GFP foci recruitment in papillar cells (+ Cas9-induced DSBs using *ry* gRNA, 106 cells, four animals; - Cas9-induced DSBs using *ry* gRNA, 36 cells, three animals; $P = 0.0092$) during the first mitotic stage. Each time point represents two or more biological replicates. Each data point represents a single animal. Error bars indicate SEM. **, $P < 0.01$ by unpaired two-tailed *t* test without Welch's correlation. (L) RPA3-GFP recruitment to + *hs-I-Crel* papillar cells after 90 min. Cells are enlarged and the channels split to show recruitment of RPA3⁺ foci to DNA. Magenta, DAPI (DNA); green, RPA3. (M and N) RPA3⁺ gH2Av⁺ foci recruitment to papillar cells post-NEBD (M) and after the first mitotic division (N) + *hs-I-Crel*. Labeling as in J except for the following: magenta, DAPI (DNA); green, RPA3; red, gH2Av.

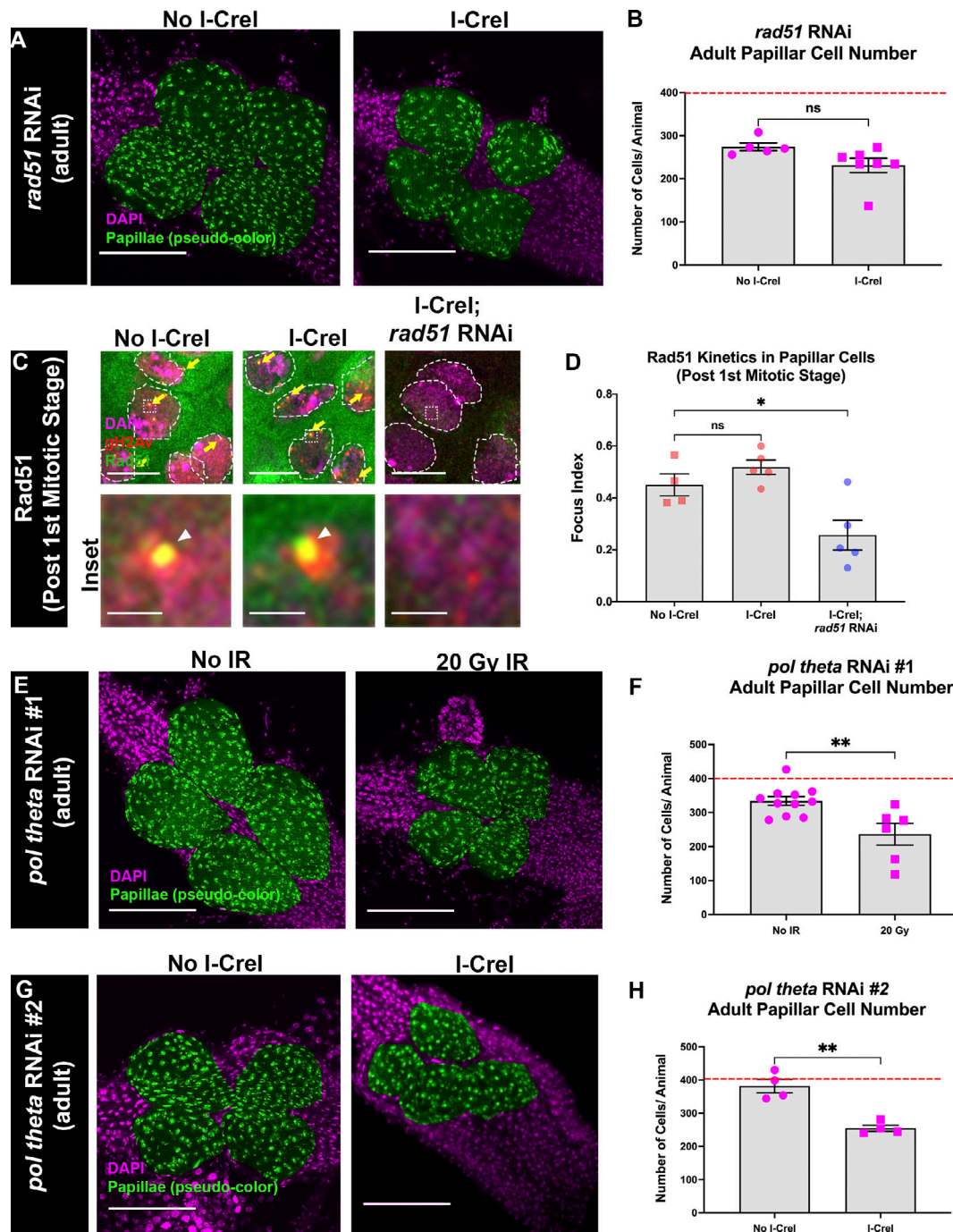


Figure S2. **Rad51 is not required for cell survival following DSBs in papillar cells.** (A) Adult rectums of *rad51* RNAi animals \pm *hs-I-Crel*. Green, pseudo-colored rectal papillae; magenta, DAPI (DNA). Scale bars = 50 μ m. (B) Quantification of adult papillar cell number in *rad51* RNAi animals (+ *hs-I-Crel*, 1,618 cells, seven animals; - *hs-I-Crel*, 1,371 cells, five animals; $P = 0.0702$). Red dashed line indicates the expected number of papillar cells in a WT adult. Each time point represents two or more biological replicates. Each data point represents a single animal. Error bars indicate SEM. Significance determined by unpaired two-tailed t test without Welch's correlation. (C) Rad51 recruitment to WT papillar cells \pm *hs-I-Crel* and *rad51* RNAi papillar cells. Yellow arrows, Rad51⁺ foci; dashed outlines, nuclei; dashed box, area magnified $\times 10$ in the corresponding inset; white arrowheads, enlarged foci. Scale bars = 10 μ m; inset scale bar = 0.5 μ m. (D) Quantification of Rad51 foci recruitment in papillar cells (+ *hs-I-Crel*, 379 cells, five animals; - *hs-I-Crel*, 193 cells, four animals; *rad51* RNAi papillar cells, 84 cells, five animals; $P = 0.0037$) after the first mitotic stage. Each time point represents two or more biological replicates. Each data point represents a single animal. Error bars indicate SEM. *, $P < 0.05$ by ordinary one-way ANOVA. (E) Adult rectums of *polQ* RNAi animals \pm IR. Labeling as in A. (F) Quantification of adult papillar cell number in *polQ* RNAi animals (+ IR, 1,418 cells, 6 animals; - IR, 3,675 cells, 11 animals; $P = 0.0043$). Red dashed line indicates the expected number of papillar cells in a WT adult. Each time point represents two or more biological replicates. Each data point represents a single animal. Error bars indicate SEM. **, $P < 0.01$ by unpaired two-tailed t test without Welch's correlation. (G) Adult rectums of *polQ* second RNAi line (RNAi #2) \pm *hs-I-Crel*. Labeling as in A. (H) Quantification of adult papillar cell number in *polQ* RNAi #2 animals (+ *hs-I-Crel*, 1,019 cells, four animals; - *hs-I-Crel*, 1,527 cells, four animals; $P = 0.0012$). Red dashed line indicates the expected number of papillar cells in a WT adult. Each time point represents two or more biological replicates. Each data point represents a single animal. Error bars indicate SEM. **, $P < 0.01$ by unpaired two-tailed t test without Welch's correlation.

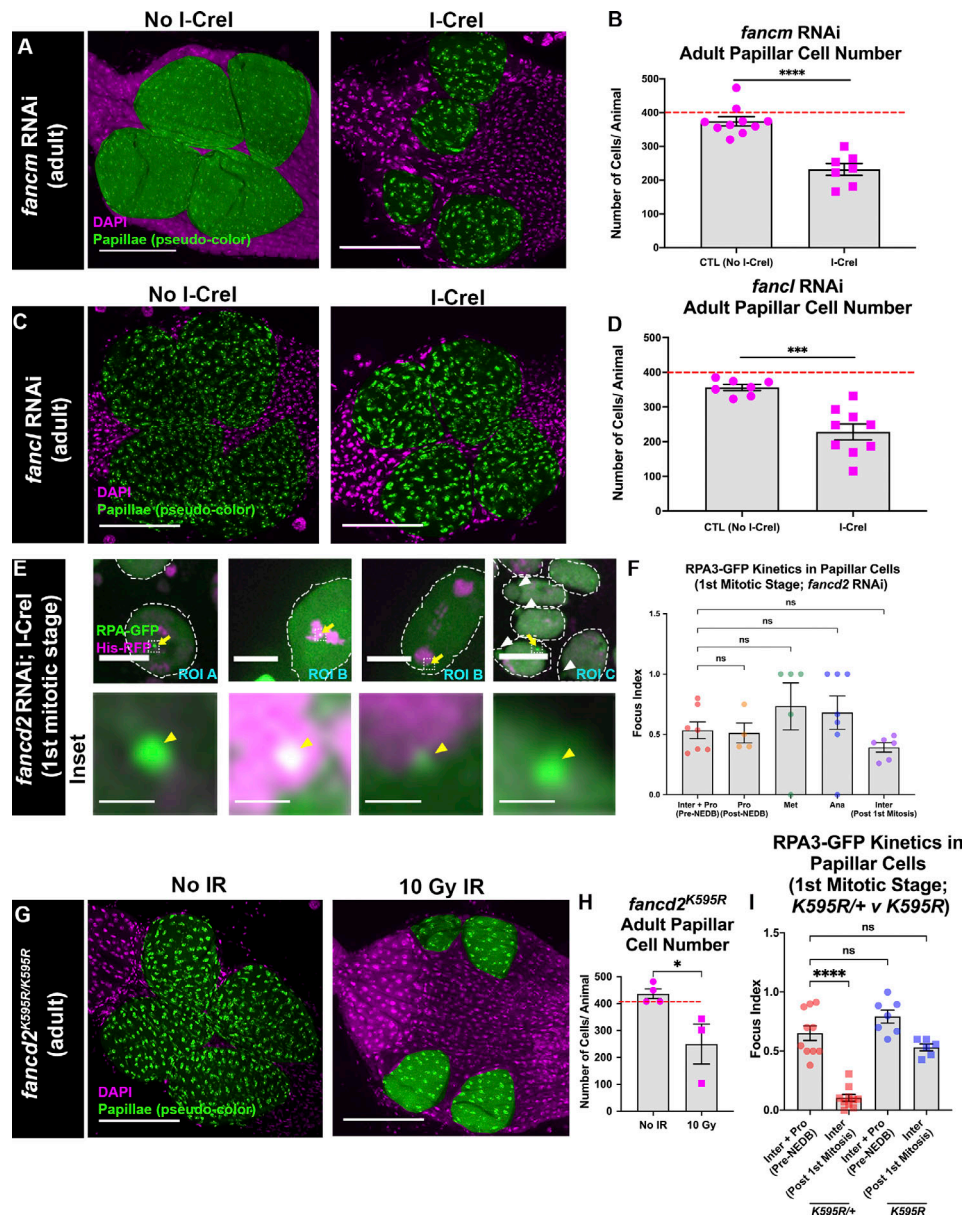


Figure S3. FA proteins are required for proper RPA3⁺ foci dynamics and cell survival following DSBs. **(A)** Adult rectums of *fancm* RNAi animals \pm *hs-I-Crel*. Green, rectal papillae (pseudocolored); magenta, DAPI (DNA). Scale bars = 50 μ m. **(B)** Quantification of adult papillar cell number in *fancm* RNAi animals (+ *hs-I-Crel*, 1,621 cells, 7 animals; - *hs-I-Crel*, 3,740 cells, 10 animals; $P < 0.0001$). Red dashed line indicates the expected number of papillar cells in a WT adult. Each time point represents two or more biological replicates. Each data point represents a single animal. Error bars indicate SEM. ****, $P < 0.0001$ by unpaired two-tailed *t* test without Welch's correlation. **(C)** Adult rectums of *fancf* RNAi animals \pm *hs-I-Crel*. Labeling as in A. **(D)** Quantification of adult papillar cell number in *fancf* RNAi animals (+ *hs-I-Crel*, 2,055 cells, nine animals; - *hs-I-Crel*, 2,493 cells, seven animals; $P = 0.0003$). Red dashed line indicates the expected number of papillar cells in a WT adult. Each time point represents two or more biological replicates. Each data point represents a single animal. Error bars indicate SEM. ***, $P < 0.001$ by unpaired two-tailed *t* test without Welch's correlation. **(E)** RPA3-GFP foci recruitment in *fancd2* RNAi expressing papillar cells \pm *hs-I-Crel*. Letters indicate separate ROIs at a given time point for a single animal. Yellow arrows, RPA3⁺ foci; dashed box, area magnified $\times 10$ in the corresponding inset; yellow arrowheads, enlarged foci; white arrowheads, micronuclei; dashed outlines, nuclei. Scale bars = 10 μ m; inset scale bar = 0.5 μ m. **(F)** Quantification of RPA3-GFP foci recruitment in *fancd2* RNAi expressing papillar cells during mitosis \pm *hs-I-Crel* (interphase [Inter] + prophase [Pro] (pre-NEBD), 280 cells, seven animals; Pro (post-NEBD), 11 cells, four animals; metaphase [Meta], 9 cells, five animals; anaphase [Ana], 12 cells, seven animals; Inter after first mitosis, 304 cells, six animals; $P = 0.7076$). Each time point represents two or more biological replicates. Each data point represents a single animal. Error bars indicate SEM. Significance determined by ordinary one-way ANOVA with Dunnett's multiple comparison test. **(G)** Adult rectums of *fancd2*^{K595R} animals \pm *hs-I-Crel*. Labeling as in A. **(H)** Quantification of adult papillar cell number in *fancd2*^{K595R} animals (+ IR, 750 cells, three animals; - IR, 1,748 cells, four animals; $P = 0.0355$). Red dashed line indicates the expected number of papillar cells in a WT adult. Each time point represents two or more biological replicates. Each data point represents a single animal. Error bars indicate SEM. *, $P < 0.05$ by unpaired two-tailed *t* test without Welch's correlation. **(I)** Quantification of RPA3-GFP foci recruitment in *fancd2*^{K595R/+} (pre-NEBD, 47 cells, 10 animals; post-NEBD, 236 cells, 8 animals) and *fancd2*^{K595R} (pre-NEBD, 76 cells, 7 animals; post-NEBD, 261 cells, 6 animals) papillar cells before and after the first mitotic division \pm *hs-I-Crel*. Each time point represents two or more biological replicates. Each data point represents a single animal. Error bars indicate SEM. ****, $P < 0.0001$ by ordinary one-way ANOVA with Dunnett's multiple comparison test. CTL, control.

Provided online are two tables as separate Word files. Table S1 lists results from a candidate screen for regulators of acentric DNA segregation during mitosis in papillar cells. Table S2 lists all the fly stocks used in this study.